Multifunctional 4D-printed sperm-hybrid microcarriers for assisted reproduction

Fatemeh Rajabasadi, Silvia Moreno, Kristin Fichna, Azaam Aziz, Dietmar Appelhans, Oliver G. Schmidt, and Mariana Medina-Sánchez**

F. Rajabasadi, A. Aziz, M. Medina-Sánchez
Micro- and NanoBiomedical Engineering Group (MNBE)
Institute for Integrative Nanosciences
Leibniz Institute for Solid State and Materials Research (IFW)
01069 Dresden, Germany

F. Rajabasadi, S. Moreno, K. Fichna, D. Appelhans
Bioactive and Responsive Polymers
Leibniz Institute for Polymer Research
01069 Dresden, Germany

F. Rajabasadi, O. G. Schmidt
Research Center for Materials, Architectures, and Integration of
Nanomembranes (MAIN)
Chemnitz University of Technology
09126 Chemnitz, Germany
E-mail: oliver.schmidt@main.tu-chemnitz.de

O.G. Schmidt
Institute for Integrative Nanosciences
Leibniz Institute for Solid State and Materials Research (IFW)
01069 Dresden, Germany

O. G. Schmidt
Nanophysics
Faculty of Physics
School of Science
Dresden University of Technology
01062 Dresden, Germany

M. Medina-Sánchez
Chair of Micro- and NanoSystems
Center for Molecular Bioengineering (B CUBE)
Dresden University of Technology
01062 Dresden, Germany

Keywords: 4D-printing lithography, biohybrid micromotors, multifunctional sperm-hybrid microcarriers, targeted cargo-delivery, assisted fertilization, enzyme-loaded polymersomes.

Abstract

Remotely controllable microrobots are appealing for various biomedical in vivo applications. In particular, our group has focused in the last years in developing sperm-microcarriers to assist sperm cells with motion deficiencies or low count (two of the most prominent male infertility problems) to reach the oocyte towards in vivo assisted fertilization. Different sperm carriers considering their motion in realistic media and confined environments have been optimized. However, the already reported sperm carriers have been mainly designed to transport single sperm cells, with limited functionality. Thus, to take a step forward, here we propose the development of a 4D-printed multifunctional microcarrier containing soft and smart materials, which can not only transport and deliver multiple sperm cells, but also release heparin and mediate local enzymatic reactions by hyaluronidase-loaded polymersomes (HYAL-Psomes). These multifunctional facets enable in-situ (i) sperm capacitation/hyperactivation, and (ii) local degradation of the cumulus complex that surrounds the oocyte, both to facilitate the sperm-oocyte interaction for the ultimate goal of in vivo assisted fertilization.

1. Introduction

A new generation of remote controllable soft and smart microrobots, propelled/guided by endogenous (e.g., chemotaxis), or exogenous (e.g., ultrasound, magnetic field, electric field) stimuli, has expanded the field of biomedical sciences by creating unique opportunities for less-invasive medical operations in vivo. Microrobots have already being used in small animals, for example, to treat stomach infection or for delivering anticancer drugs.[1–6] These microrobots are characterized by their propulsion mechanism, which may be chemical, physical, or biohybrid.[7] In particular, microrobots propelled by motile cells or microorganisms have been widely used, as they take advantage of the taxis and cell-interaction abilities of the living components with the control/steerability and the imaging enhancement of the synthetic microparts.[8]

Among different types of motile microorganisms and cells, bacteria and spermatozoa are promising candidates for delivering therapeutic cargoes. This is due to their very efficient propulsion mechanism, flagellum beating, which allows them to adapt to different microenvironments and to swim in complex fluids—even against the flow.[9–11] Among bacterial strains, *Magnetococcus marinus* "MC-1", known as magnetotactic bacteria (MTB), has been used for drug-delivery applications, as it can be genetically modified using tools of synthetic biology to improve its targeting ability and to reduce its pathogenic nature.[12–16] Additionally, the magnetosomes in the *M. marinus* cell not only offer the possibility of external magnetic guidance, but also enable their tracking via magnetic resonance imaging (MRI).[2,17]

Spermatozoa (sperm cells) are other promising biological components for constructing biohybrid microrobots, as they are inherently optimized to swim through complex fluids and organs, such as those in the reproductive system, without producing harmful immunoreactions. Besides their natural function of fertilization, sperm cells exhibit a high drug encapsulation capability along with a high drug carrying stability, which makes them suitable for various gynecological healthcare applications.[18,19] Moreover, their chemotaxis (tendency to swim toward a higher concentration of extracellular signals), thermotaxis (tendency to swim towards a temperature gradient), thigmotaxis (tendency to swim near the surface), and rheotaxis (swimming against the fluid flow), abilities offer a wide range of options for their motion control, making them promising medical vehicles for minimally-invasive operations.[20–26]

Our group was the first to employ sperm cells as components of microrobotics systems,[18] in particular towards the development of novel in vivo assisted fertilization methods, where sperm cells with motion deficiencies (asthenospermia) or low count (oligospermia) could be assisted by engineered microrobots.[27,28] In fact, the capture, guidance and release of single sperm cells employing different synthetic microstructures have been demonstrated.[19] Optimizations on the microstructures geometry have also been carried out, considering parameters such as sperm morphology and tail beating amplitude, as well as, the temperature and viscosity of the surrounding fluid.[29,30] Furthermore, the release of a single sperm cell has been demonstrated using either thermo-responsive rolled-up microtubes, or tetrapod-like microstructures with bending arms.[31,32] In the case of motion deficient sperm cells, micropropellers based on helical structures were developed to perform cargo delivery to the oocyte,[27] or more recently sperm were decorated with magnetic particles for their propulsion under oscillating magnetic fields.[19,33]

The vision of this project is to assist sperm cells to reach the fertilization site in in vivo scenarios, when the sperm count is low (<20 million sperm per mL), also called oligospermia. Current treatments for this male infertility problem are based on in vitro fertilization (IVF) and intracytoplasmic sperm injection (ICSI). The first one consists of incubating the preselected sperm cells (millions of them) nearby the retrieved oocytes. On the other side, in ICSI just one sperm is picked up and directly injected into the oocyte cytoplasm. In both cases, the fertilization rates are quite high, above 93.4% based on the German register for IVF procedures.[34] However, the problem persists when looking at the embryo implantation rates, which are 26.3% and 29.4% after the transfer of a 1-day and 5/6-day cultured embryo, respectively. These low implantation rates might be due to the oxidative stress that gametes experience during retrieval, washing, selection, and incubation steps, processes that are known to affect gamete quality. Thereupon, we aimed to assist those sperm cells in vivo conditions to perform the fertilization process under more natural conditions. To accomplish this goal, we are developing different approaches to transport a high number of sperm cells as well as to increase the functionality of the microcarrier.

Here, we employ both a non-stimuli-responsive polymer (IPS photoresist) and a thermo-responsive hydrogel poly(N-isopropylacrylamide) (PNIPAM), for the fabrication of 4D printed sperm microcarriers via two-photon polymerization (TPP) **(Figure 1a)**. In our recent review article, the fundamentals of 3D and 4D lithography of untethered microrobots were comprehensively reviewed.[35] Among the stimuli-responsive materials, hydrogel-based

polymers are versatile as they can undergo reversible solubility transition upon application of certain stimuli (e.g., temperature, salt concentration, pH).[36] One of the most well-studied stimuli-responsive hydrogels is PNIPAM, which responds to temperature changes. Its thermo-responsiveness is based on a reversible phase transition from a swollen hydrophilic state at temperatures below its lower critical solution temperature (LCST) to a collapsed hydrophobic state at temperatures above its LCST.[37–41] Therefore, we hereby used PNIPAM to equip the microcarriers with soft and smart microgates for triggering the release of heparin and motile sperm cells, for future in vivo assisted fertilization. Moreover, we functionalized the microcarriers with a specific nanocarrier platform to locally mediate the degradation of hyaluronic acid (HA) found in the oocyte-cumulus complex.[42,43] Thus, by taking advantage of smart materials and novel microfabrication techniques, we present here a multifunctional microcarrier able to: (i) transport and deliver multiple motile sperm cells, to increase the chances of fertilization, (ii) in-situ capacitate/hyperactivate the sperm cells through the local release of heparin, and (iii) assist the degradation of the HA-cumulus complex, by the local action of HYAL-Psomes previously functionalized on the microcarrier's surface. The microcarriers are also coated with a metallic layer (Au) to enhance their visualization via dual ultrasound (US)/photoacoustic (PA) imaging, which makes them potential candidates for future in vivo applications.

2. Results and Discussion

2.1. Concept and fabrication of the 4D-printed microcarriers

In this work, a modified protocol for the synthesis of PNIPAM was employed **(see the Experimental Section in the Supplementary information)**.[44] The whole fabrication process of the proposed microcarrier is depicted in **Figure 1a**, comprising the following steps: fabrication of the supporting structure, patterning of the thermo-responsive microgate, coating with metal-oxide for magnetic guidance and imaging contrast enhancement, and two final functionalization steps to load heparin into the PNIPAM microgate and to immobilize HYAL-Psomes onto the microcarrier's surface. In **Figure 1b,i,** the optical microscopy image shows the microcarrier coupling with multiple motile sperm cells. In the fluorescence microscopy image, both the non-stimuli-responsive (passive) and stimuli-responsive (active) components of the microcarrier are distinguishable **(Figure 1b,ii)**. The green color represents IPS photoresist, a non-stimuli-responsive material which is autofluorescent, and the red color represents PNIPAM, a thermo-responsive hydrogel which was mixed with Rhodamine B (RhB) prior polymerization.

Bovine sperm cells were chosen due to their availability and similar morphology to human sperm cells. All mammalian sperm cells consist of a head, a midpiece, and a flagellum. Bovine sperm cells are about 60–70 μm long including the sperm head which is approximately 10 μm long and 5 μm in diameter. The head has an oval, flat shape and is approximately 1 μm in thickness.[45] Therefore, the microcarrier was designed with multiple cavities, each of them with an overall size of 8×8 μm^2. The cavities can be observed in the scanning electron microscopy (SEM) image **(Figure 1b,iii)**. This microfabrication design enables us to keep the captured sperm cells inside the microcarrier during transport while propelling it via the sperm cells' tail beating. Furthermore, we considered previous hydrodynamic studies on different sperm-hybrid microrobot "spermbots", in which the stream-lined cap design resulted in efficient spermbot motion, even in ex vivo oviduct fluid and highly viscous medium.[30] The general concept of the suggested multi-material microcarriers is shown in **Figure 1c**. In **Figure 1d, i-ii**, the biocompatibility of all employed components of the microcarrier was assessed using a MTS-Assay, confirming that there was no significant effect on Madin Darby Canine Kidney (MDCK) cells' viability (**details in the Supplementary information**). Regarding the potential inflammatory response of the sperm microcarriers, a previous study by our group shows that after incubating the microcarriers in ex vivo human whole blood,[46] no coagulation and granulocyte activation indicators were present in comparison with the bare control sample (only blood), demonstrating that neither a specific immune response nor inflammation was induced by sperm or the sperm microcarriers. This experiment was done using Chandler loops (which employs an ELISA assay), where the blood was incubated with sperm cells and microrobots for 2 h. Also, cytotoxicity assays employing sperm and various sperm carriers have been performed in previously published works of our group, showing a non-evident cytotoxicity effect.[27,32]

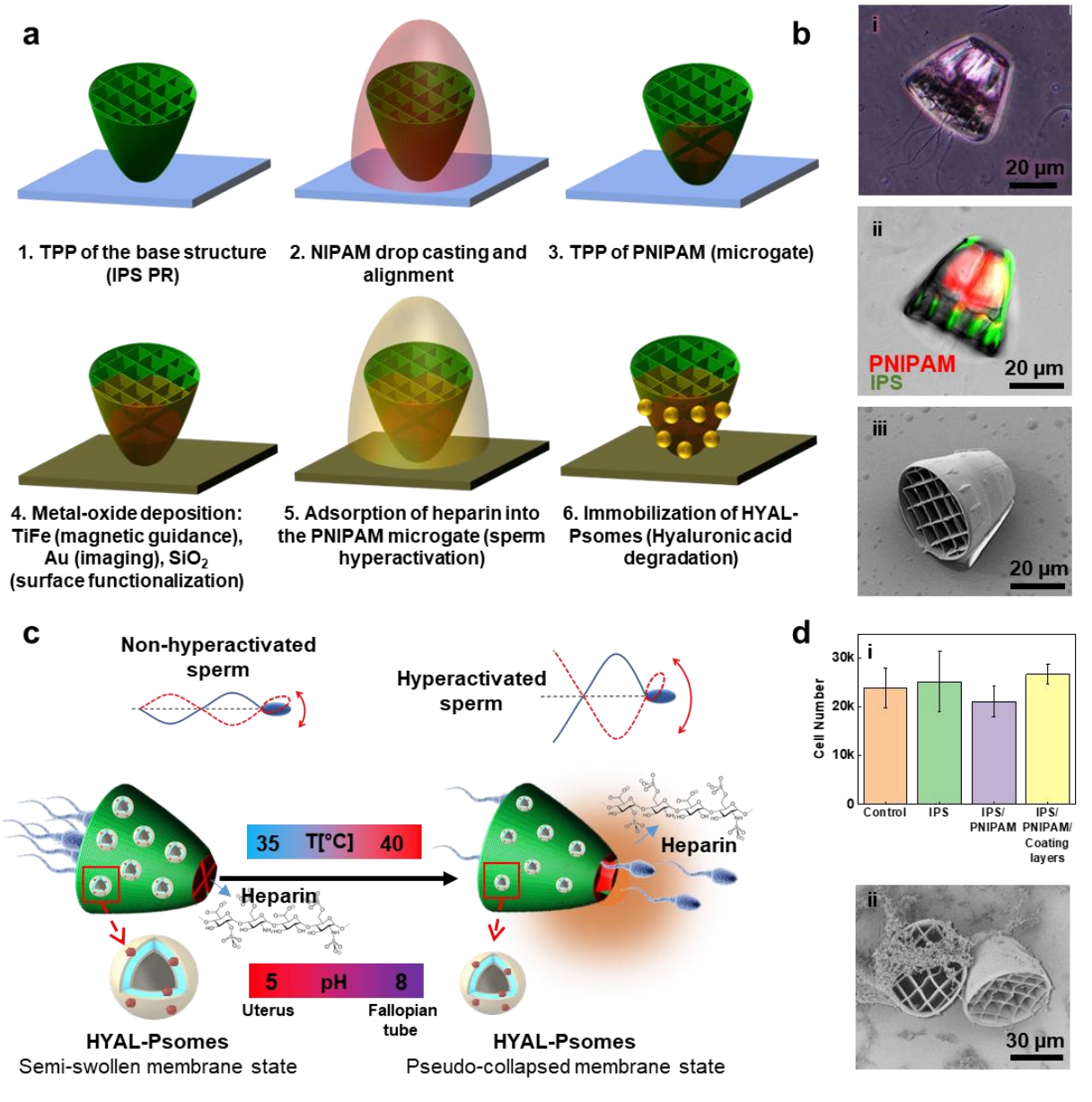

Figure 1. a) Fabrication steps of the 4D-printed microcarrier, 1. TPP of IPS photoresist (base structure), 2. Drop casting of PNIPAM and alignment, 3. TPP of PNIPAM (microgate), 4. Coating Ti/Fe/Au/SiO_2 onto the microcarriers for further magnetic guidance/imaging/surface functionalization, and two functionalization steps: 5. Heparin loading into the polymeric networks of PNIPAM, and 6. Immobilization of HYAL-Psomes on the microcarrier's surface, b) (i) Optical microscopy image of the resulting microcarrier with captured multiple motile sperm cells, (ii) Fluorescence microscopy image showing both the passive (green) and active (red) components of the microcarrier, and (iii) Corresponding SEM image highlighting the cavities where sperm cells will be coupled, c) Concept of the multifunctional microcarrier with heparin (used for sperm hyperactivation) and hyaluronidase (used for cumulus cell removal), and the expected natural stimuli (pH and temperature varying from the uterus to the fertilization site), d) Biocompatibility test, (i) MTS-assay results which show biocompatibility of

microcarrier components (n=5000, N=6, mean, ±SD), and (ii) SEM image of MDCK cells in contact with microcarriers.

2.2. Characterization of the 4D-printed stream-lined microcarriers

As explained above, the proposed 4D-printed stream-lined microcarrier, consisting of a base microstructure made of passive photoresist IPS (non-stimuli-responsive) and an adaptable microgate made of active PNIPAM hydrogel (thermo-responsive), was fabricated via TTP.

The geometry of the microcarrier was designed by considering previously reported works of our group, in which the performance improvement of the stream-lined cap compared to the cylindrical one was analyzed. [30,47] As expected, the tubular microrobot was more prone to obstruct by the obstacles in the fluid, compared to the stream-lined cap which experienced lower hydrodynamic pressures and a stable wake flow around it. This characteristic makes the stream-lined cap to consume lower energy to swim forward which leads to less consumption of the sperm's energy. We summarized the process of the geometrical optimization of microcarrier in **Figure S1 (detail information and results can be found in the Supplementary information)**.

In order to optimize the response of the PNIPAM microgate, different parameters were considered during the fabrication of the structures, namely the laser power (LP) and the scan speed (SS). These two parameters regulate the local exposure dose which affects the degree of hydrogel cross-linking.

First, cubic microstructures with the size of $30 \times 30 \times 10\ \mu m^3$ were fabricated using different LP and SS. After polymerization, the sample was developed and tested by using a Peltier element mounted underneath the sample to change the temperature of the solution in which the structures were immersed **(detail in Supplementary information; Video S1)**. It is known that high cross-linked polymer results from a high exposure dose either by increasing the LP or the time of exposure (decreasing the SS), leading to a lower temperature response (referred to as hard cube).[44] Likewise, using lower LP or higher SS (lower exposure dose) results in a lower cross-linked polymer with higher thermo-response (referred to as soft cube) **(Figure 2a, i-ii)**. These varying parameters allow us to exploit a variety of thermo-responsive properties within the same material **(Figure 2a, ii)**. **Figure 2a, iii** shows the reversible shape change of the soft cube with maximum response upon temperature change.

In this work, the PNIPAM microgate was fabricated in three dimensions (3D), so the effect of varying heights (corresponding to the volume) on its thermo-responsive properties was also

studied. Based on a previous study conducted by Hippler and colleagues, the thermal expansion coefficients and Young's modulus of PNIPAM depend significantly on the structure volume.[44] To investigate this effect, different cubic microstructures with different heights were fabricated (within the size range of the required microgate, see **Figure 2b**). **Figure 2b** demonstrates that when the height of the PNIPAM cubes increases, the thermo-response of the cubes also increases from ca. 700 μm^2 (in cubes with a height of 10 µm) to ca. 1400 μm^2 (in cubes with a height of 30 µm), almost doubling. Based on these results, we can conclude that the thermo-response of PNIPAM is in all dimensions, and the shape changes are also more pronounced when the volume of the polymeric structure is higher.

The initial characterization of the 3D-printed PNIPAM microstructures was carried out in the temperature range from 25°C to 40°C to observe the thermal actuation of PNIPAM in the whole range to identify the lower critical solution temperature (LCST) of the 4D printed microstructures. Then, by knowing the thermo-responsive properties of PNIPAM at the microscale, the design of the microgate for the release of multiple sperm cells was optimized. The microgate has to guarantee the prevention of unwanted sperm release during transport and provide enough space for releasing them at the physiological temperature (ca. 38°C, in the luteal phase before fertilization).[48] To accomplish this goal, different designs for the microgate were investigated (**Figure 2c, i-iii; Video S2)**. After several design optimizations, and based on the size of the sperm head (10×5 μm^2), design number (**Figure 2c, iii**) was the most promising, exhibiting major shape change, thus ensuring enough space for the sperm release. In **Figure 2c, iv** the microcarrier components in the microgate area are shown under fluorescence microscopy, where we can distinguish the active part (PNIPAM) from the passive part (IPS) with different colors, red and green, respectively. Here the height of the PNIPAM was ca. 15 µm, which was a good compromise for the overall size of the microstructure and the response needed for the particular task of sperm release. In the same figure, the thermo-response of the final microcarrier design in the swollen (at 25ºC), and the shrunken (at 40ºC) state of its microgate is depicted **(Video S3)**.

Since the fabricated microcarriers are intended to be used in physiological fluids, including the oviduct fluid with viscoelastic properties, we tested the thermo-response of the chosen microgate design in different media such as water, sperm medium (SP-TALP), and SP-TALP enriched with 0.2% Methylcellulose (MC) (the latter mimicking the rheological properties of ex vivo oviduct fluid in the luteal phase) **(detail in Supplementary information; Figure 2d)**.[30] As expected, the thermo-response of the microgate was affected by the viscosity of the

medium, probably due to the different diffusion rates within the polymeric-network of PNIPAM.[49] According to **Figure 2d, iii,** the resulting shape change of the microgate at the physiologically relevant temperature range (from 35°C to 40°C) **(detail of the chosen range in the supplementary information)** and in the mimicking oviduct fluid (SP-TALP enriched with 0.2% MC) was ca. 45-60 µm^2, which was sufficient for the sequential release of individual sperm cells.

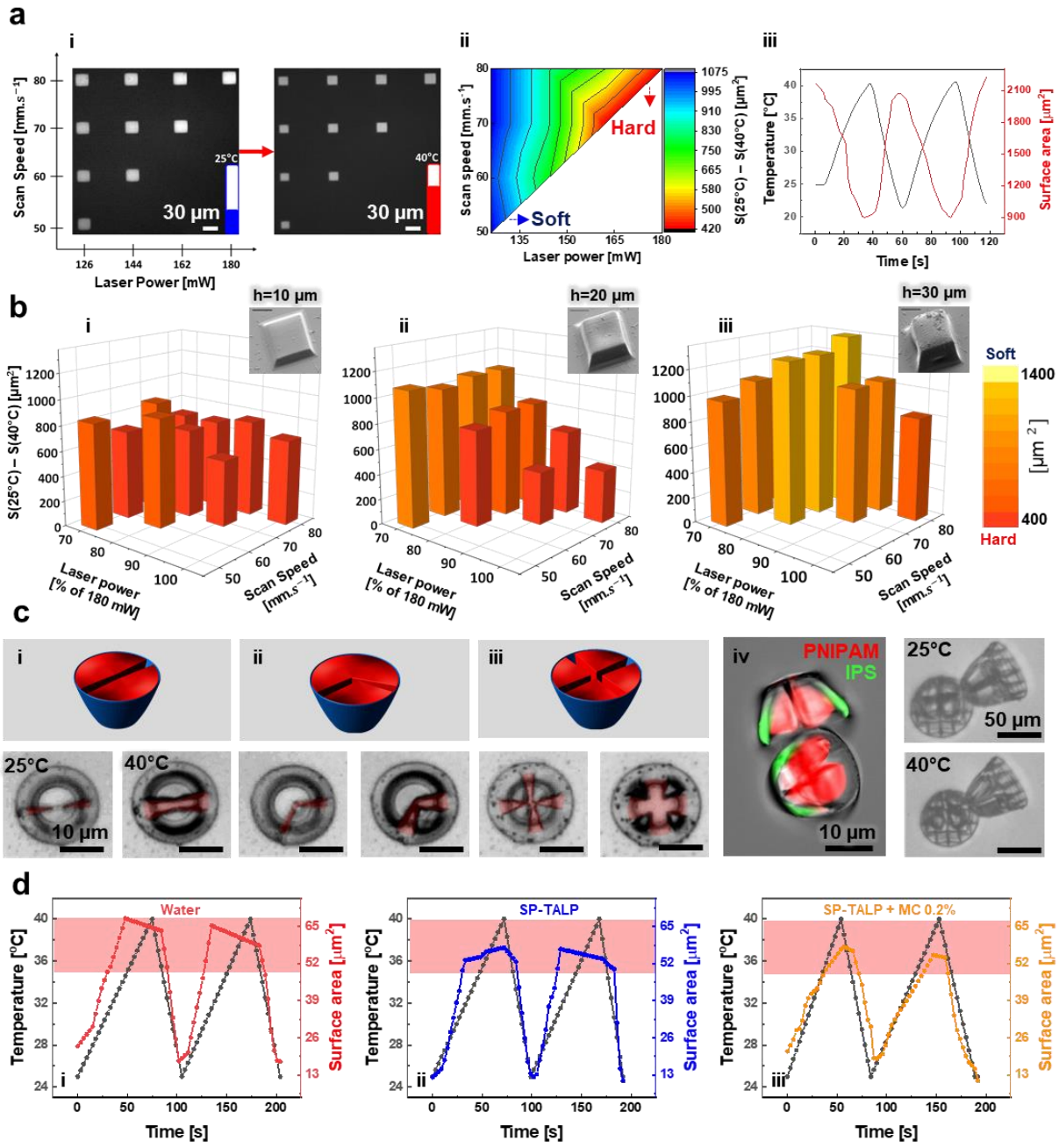

Figure 2. a) Bulk temperature actuation test, (i) PNIPAM cubes with length of 30 µm and height of 10 µm in the swollen state (25°C) and shrunken state (40°C), (ii) Surface area changes of the cubes with different writing parameters, red color shows higher cross-linked polymers/less temperature-response

(hard) and blue color shows lower cross-linked polymers/high temperature-response (soft) (n=1 per each LP and SS, N=1 cycle), (iii) Shape changes of the soft cube over time and temperature changes (25°C–40°C) (n=1, N=2 cycles), b) Surface area changes of cubes with the length of 30 μm and height of 10 μm, 20 μm, and 30 μm, the yellow color is represented the high thermo-responsive PNIPAM cube (soft) and the red color is represented the less thermo-responsive PNIPAM cube (hard), by increasing the volume of PNIPAM, the shape changes are more pronounced (n=1 per each LP and SS, N=1 cycle), c) (i–iii) Three different investigated designs for the microgate of the microcarrier in two different states, swollen (25°C) and shrunken (40°C), and (iv) The fluorescence microscopy image of two existing components of the microgate (red color represents PNIPAM and green color represents IPS). Here surface area change is the area indicated in transparent-red in Figure 2c.iii (n=1, N=2 cycle). d) Temperature actuation test of the optimized gate design (c, iii) in different media: (i) water, (ii) SP-TALP, and (iii) SP-TALP enriched with 0.2% MC. (n=1, N=2 cycle). The transparent-red region highlights the physiological temperature range and the corresponding surface area change, which is then used for the consequent experiments.

2.3. Microcarrier loaded with heparin for in situ sperm capacitation

For a successful fertilization process, sperm cells have to overcome different biological barriers to finally reach the oocyte. Sperm cells have to be capacitated/hyperactivated to be able to penetrate the oocyte zona pellucida. Hyperactivation may also facilitate sperm cell release from the oviductal storage reservoir.[50] In this regard, heparin has been widely used for sperm capacitation in vitro, when the natural environment is not available, as it induces biochemical modifications that allow sperm cells to acrosome react upon exposure to the zona pellucida, cumulus complex, and other substances associated to in vitro matured oocytes.[51]

As we aimed to facilitate sperm migration, and since PNIPAM can adsorb aqueous solution, we loaded heparin into the PNIPAM microgates when they were immersed in TALP solution (SP-TALP without bovine serum albumin (BSA) which triggers capacitation).[52,53] The loading was carried out when the PNIPAM microgates were in the hydrophilic phase (swollen state, at room temperature) **(details in the Supplementary information)**. The loaded heparin was then released upon temperature increase (when PNIPAM shrank, the adsorbed aqueous-solution was expelled from its polymeric network). Thus, the sperm cells which were in contact with the heparin in the surrounded medium were locally capacitated/hyperactivated (conceptual image shown in **Figure 3a**). The fluorescence microscopy images (the bright field and fluorescence channels) show the heparin loading into the PNIPAM microgate **(Figure 3b)**.

To estimate the concentration of loaded-heparin per each microcarrier and its effect on sperm hyperactivation, we performed different experiments. First, the effect of different concentrations of heparin (0, 0.025, 0.1, 0.25 mg mL^{-1} in SP-TALP) on sperm motion behavior was tested. In agreement with Magdanz's work, at 0.1 mg mL^{-1} of heparin, we obtained the maximum average path and curvilinear velocity of sperm cells **(Figure 3c, i)**.[54] The increases in average path velocity in the presence of heparin were not significant because sperm hyperactivation is followed by asymmetric tail beating with high amplitude and aggressive head motion, which we observed by a pronounced increase in the curvilinear velocity. This concentration was therefore considered optimal for subsequent experiments.

Next, we evaluated the effect of temperature on sperm mean velocity, as here the trigger to release heparin from the PNIPAM microgate was enacted by a temperature change, in contrast to the aforementioned work, in which the trigger was enacted by a pH change **(Figure 3c, ii)**. By increasing the temperature from 35°C to 40°C (the physiologically relevant temperature range), sperm velocity increased from ca. 34 to ca. 78 µm s^{-1} in sperm media without heparin and from ca. 43 to ca. 103 µm s^{-1} in sperm media containing 0.1 mg mL^{-1} heparin, meaning a 17% increase in velocity in the presence of heparin. Here the most dominant effect on sperm velocity came from temperature. Due to the physiological properties of sperm cells, described by Rikmenspoel in 1984, sperm metabolism is accelerated by an increase in temperature, altering both the frequency and amplitude of sperm tail beating.[55] The influence of temperature on sperm velocity is reported in the previous work of our group.[28] In **Figure 3c,iii**, one can see the capacitation/hyperactivation of both parameters, temperature and heparin, in the increased number of sperm cells which swam in circular trajectories. Moreover, sperm motility was also investigated **(Figure S2)**. As expected, at a higher temperature, sperm cells lose their motility faster than at a lower temperature because of the higher swimming speed and energy consumption rate **(Figure S2a)**. This reduction was even more pronounced when the sperm cells were capacitated/hyperactivated **(Figure S2b)**. Thus, it can be assumed that hyperactivation has a significant effect on sperm motility by increasing the rate of energy consumption and therefore reducing their lifetime.

After loading the microcarriers with heparin, a quantitative toluidine blue assay was carried out to determine the concentration of heparin per microcarrier **(detail in Supplementary information)**. As shown in **Figure 3d, ii**, by increasing the temperature, PNIPAM was gradually shrunk, enabling heparin release. While maintaining a constant temperature of 40°C, heparin release was measured at different time intervals. After 15 min there was no change in

the absorbance value, indicating that no further heparin was released **(Figure 3d, iii)**. According to the absorbance results and the calibration curve in **Figure 3d, i**, the concentration of loaded heparin per microcarrier was calculated to be 0.465 pg.

Finally, the effect of the microcarrier-released heparin on the surrounding sperm cells was investigated **(Figure 3e)**. In the first set of experiments (left columns) in **Figure 3e.i**, on sperm solutions with and without 0.1 mg mL^{-1} heparin, the increase in sperm velocity followed the same trend as shown in **Figure 3c**. At physiological temperature, the sperm velocity increased 2.3 times when the sperm solution contained 0.1 mg mL^{-1} of heparin. In the second set of experiments (right columns), we measured the sperm velocity in the presence of microcarriers with and without heparin (free sperm cells in the solution were considered). When the microcarriers were not loaded with heparin, the sperm velocity was similar to that of the free-swimming sperm cells without heparin. In the case of microcarriers loaded with heparin, as the temperature was raised to trigger the release of heparin, sperm velocity increased **(Figure 3e, i)**. Consequently, in **Figure 3e, ii**, the effect of heparin on the motion trajectory of the sperm cell was demonstrated. The motion trajectories of sperm cells at room temperature (25°C) and physiological temperature (38°C), with and without heparin in the solution, reveal the fact that both temperature and heparin have a positive effect on the sperm capacitation/hyperactivation. The hyperactivated sperm cells are intended to swim in a circular motion pattern because of an increase of amplitude and asymmetrical tail beating (**Video S4**).

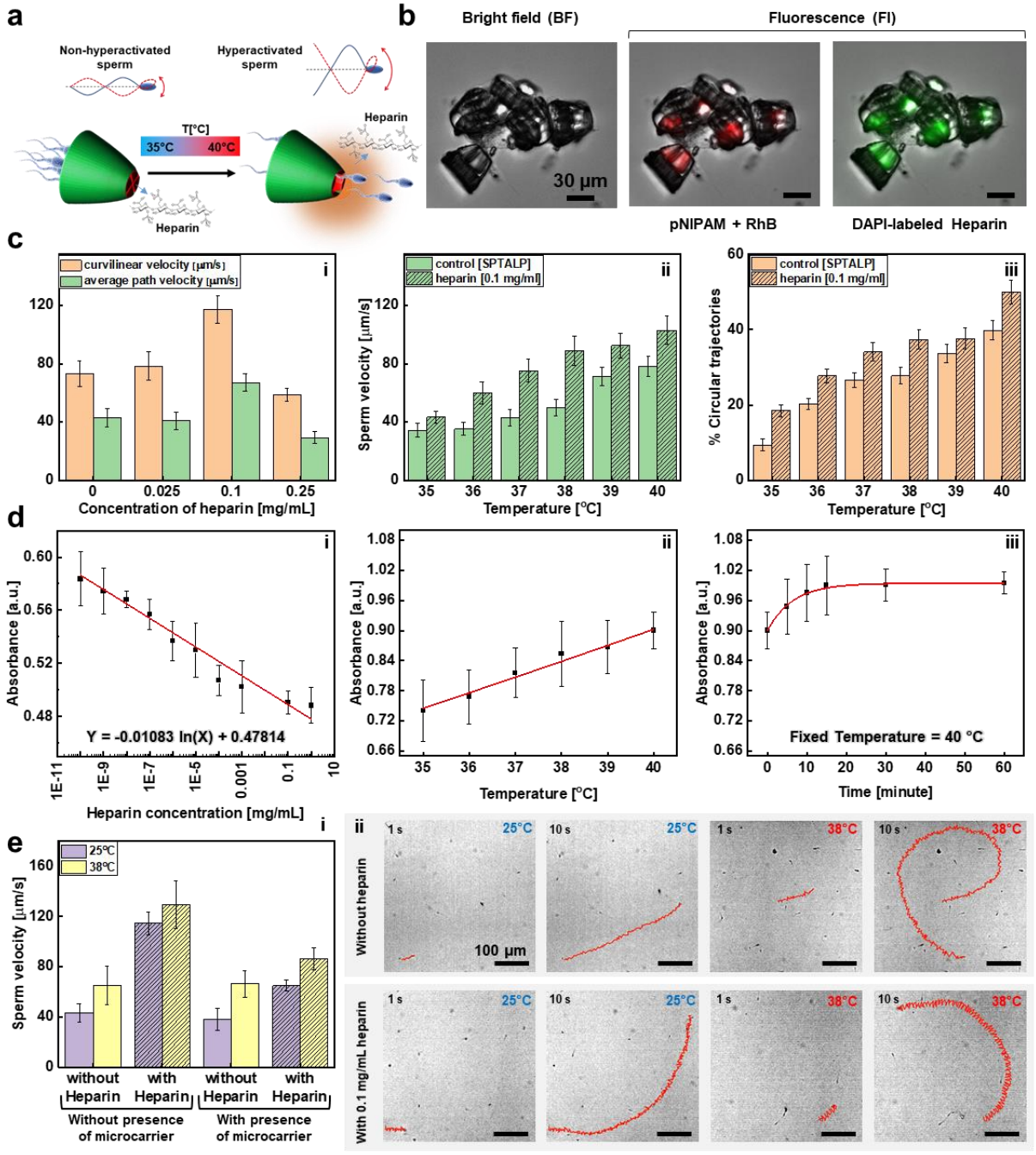

Figure 3. a) Conceptual schematic of heparin release and sperm hyperactivation, b) Fluorescence microscopy images show the presence of heparin loaded in the PNIPAM microgates, red channel represents the PNIPAM gates (presence of RhB) and green channel represents the loaded heparin, c) (i) Curvilinear and average path velocity of free sperm cells in different concentrations of heparin in SP-TALP (n=200, N=3, mean, ±SD), (ii) Effect of 0.1 mg mL^{-1} heparin on sperm velocity at different temperatures (n=200, N=3, mean, ±SD), (iii) Percentage of sperm cells with circular trajectories with and without the presence of heparin in SP-TALP (n=200, N=3, mean, ±SD), [analyzed by SCA® CASA System for semen analysis], d) (i) Calibration curve of heparin based on toluidine blue assays, and Accumulative heparin release from microcarriers at (ii) different temperatures ($n_{microcarrier}$=1500, N=3,

mean, ±SD), and (iii) time durations ($n_{microcarrier}$=1500, N=3, mean, ±SD), [absorbance at 631 nm], e) (i) Effect of released heparin from microcarriers on sperm velocity at room temperature (25°C) and physiological temperature (38°C) (n=200, $n_{microcarrier}$=20, N=3, mean, ±SD), [analyzed by SCA® CASA System for semen analysis], (ii) The motion trajectory of non-hyperactivated and hyperactivated sperm at room temperature and physiological temperature with and without heparin in the solution. In all experiments containing sperm, we used washed sperm which had not undergone any preselection process, e.g., swim-up, to avoid any sperm capacitation and only monitor the effect of heparin.

2.4. Microcarriers decorated with hyaluronidase post-loaded polymersomes (HYAL-Psomes) for in situ degradation of the HA-cumulus complex

Hyaluronidase (HYAL) is a hyaluronic acid-containing sperm acrosomal enzyme that plays an important role in the fertilization process through its participation in the degradation of the extracellular matrix (ECM) of the cumulus cells.[56] In in vitro fertilization (IVF) and intracytoplasmic sperm cell injection (ICSI), HYAL is used to remove the cumulus cells around the oocytes.[35] We intended to address infertility-related lack of HYAL, caused by low sperm count, by adding HYAL onto the microcarrier in order to help sperm cells digest the cumulus cells—the final barrier to fertilization. For this purpose, we proposed a novel nanocarrier platform based on polymersomes (Psomes) for post-loading of HYAL, as Psomes are further immobilized onto the microcarrier's surface. Psomes are prepared based on the self-assembly of amphiphilic block copolymers which provide them with excellent mechanical and chemical stability. Moreover, Psomes' membrane permeability can be triggered by external stimuli (e. g., pH, temperature, redox potential, light, magnetic field, and ultrasound).[57] This platform allowed us to uniformly immobilize enzymes onto the microcarrier's surface while preserving their activity.

2.4.1. HYAL-Psomes preparation and characterization

First, pH-responsive and photo-crosslinked Psomes were synthetized by self-assembly of block copolymers (BCPs) using the so-called pH switch method **(Figure S3; detail in Supplementary information)**.[58–60] The chemical structure, composition, molar mass and dispersity of the BCPs used are listed in **Table S1**. Then, hyaluronidase was integrated into the membrane of the Psomes using a recently established protein post-loading approach **(Figure 4a; detail in Supplementary information)**.[61] Here, different characterization approaches were conducted to measure loading efficacy, such as the particle shape, size, and membrane thickness of Psomes before and after enzyme loading (Empty-Psomes, and HYAL-Psomes)

(Table 1). We employed cryogenic transmission electron microscopy (cryo-TEM) and compared the results with dynamic light scattering (DLS) measurements. As one can see in **Table 1**, the increase in diameter confirms the successful loading of HYAL; however, there is no difference in membrane thickness, for which two explanations are proposed: either the enzyme is attached to the Psomes' surface, or it is too small to change the membrane thickness.[60] Furthermore, the pH cycles and pH titration of Empty-Psomes and HYAL-Psomes with DLS were also considered to check reversible pH-response and the swollen/collapsed states of Psomes before and after the loading process **(Figure S4**; **Table S2)**.

Table 1. Diameter and membrane thickness of Empty-Psomes (before post-loading) and HYAL-Psomes (after post-loading) with cryo-TEM and DLS. (C_{Psomes} = 0.5 mg mL^{-1}, C_{HYAL} = 0.2 mg mL^{-1}, 1 mM PBS) at pH 8. DLS measurements were carried out in triplicate. Calculated values using cryo-TEM images were obtained by analyzing 60 particles.

	Empty-Psomes Before post-loading	HYAL-Psomes After post-loading
Diameter by DLS [nm]	78.0 ± 0.9	85.1 ± 1.8
Diameter by cryo-TEM [nm]	70.8 ± 7.2	82.6 ± 4.9
Membrane thickness [nm]	14.0 ± 1.1	14.0 ± 0.8

To estimate the loading efficiency of HYAL-Psomes, we used labeled enzymes (here we used RhB) **(Figure S5)** with the same post-loading process and preparation of the solution as naked enzymes **(detail in Supplementary information)**. The calibration curve of the used RhB-SCN is depicted in **Figure S6**. The loading efficiency was carried out after the purification process of RhB-HYAL-Psomes (during the dialysis process, unloaded RhB-HYAL was defused out because of its smaller size) **(Figure S7a, i)**. Next, the absorbance of the solutions per purification day was measured (the absorbance peak correlated to the amount of RhB in the solution). The maximum loading efficiency was ca. 41% **(Figure S7a, ii)**, and the average loading efficiency for at least 10 experiments was ca. 28% **(Figure S7a, iii)**.

The enzymatic activity of HYAL-Psomes was also evaluated after purification, and considering different storage conditions via optical density measurement **(Figure S7b; detail in Supplementary information)**. For this purpose, the enzymatic activity was compared with the calibration curve of fresh free HYAL and unpurified HYAL-Psomes **(Figure S8)**. The residual enzymatic activity of HYAL-Psomes after 72 H was approximately 20%, which agrees with the above-mentioned loading efficiency experiments estimated by fluorescence spectroscopy. In the same graph, the enzymatic activity of HYAL-Psomes under different storage conditions

(fridge (4°C), and freezer (-20°C)) is also depicted **(Figure S7b)**. Based on these results, both storage methods, fridge and freezer, can be recommended as promising long-term storage condition.

Finally, HYAL-Psomes showed satisfactory stability under pH changes which naturally occur in the female reproductive tract (pH ~ 4.4 in the vagina, pH ~ 7-7.2 in the uterus, pH ~ 7.9 in the oviduct) **(Figure S7c, i**), with no significant HYAL release **(Figure S7c, ii)**. Thanks to this characteristic, HYAL-Psomes are suitable candidates to mediate degradation of the HA-cumulus complex, with the vision of facilitating sperm journey to the oocyte in future in vitro and in vivo fertilization experiments.[62,63]

2.4.2. Immobilization of HYAL-Psomes on the microcarrier's surface

The immobilization of HYAL-Psomes on the microcarrier surface based on a non-covalent interaction between β-cyclodextrin (β-CD) (on the microcarrier surface) and polyethylene glycol (PEG) chains of Psomes, was carried out as shown in **Figure 4b (detail in Supplementary information)**. To confirm Psomes immobilization onto the microcarrier surface, different characterization methods were employed. In the confocal laser scanning microscopy (CLSM) images, in which we used RhB-HYAL-Psomes for better visualization, one can see that the microcarrier surface was uniformly decorated by RhB-HYAL-Psomes **(Figure 4c)**. To validate those results, SEM imaging was performed, in which we observed a rough and heterogeneous surface of the functionalized microcarrier due to the presence of the HYAL-Psomes, compared to the smooth surface of the non-functionalized microcarrier **(Figure 4d)**. The cryo-TEM images in **Figure 4e** show spherical objects representing Empty-Psomes and HYAL-Psomes on the microcarrier surface with a quite uniform shape and size following immobilization.

Finally, as a proof of concept, the interaction between HYAL-Psomes and isolated cumulus cells (HA-cumulus complex) was investigated **(Figure 4f)**. The first two images show only the HA-cumulus complex in the IVF medium after 30 min of incubation at 38°C (in in vitro fertilization of bovine gametes, it is recommended to expose cells to high concentrations of hyaluronidase (50-250 IU mL^{-1} ~ 0.06-0.3 µg mL^{-1} for ca. 30 min).[64] There was no obvious evidence of HA-cumulus complex degradation after 30 min of incubation. The second experiment was conducted with 0.04 µg mL^{-1} hyaluronidase in the IVF solution, in which the cumulus cell cluster disintegrated into small pieces after 30 min of incubation. As a third experiment, we considered non-loaded microcarriers with HYAL-Psomes (ca. 50

449 microcarriers). In that experiment, there was no evidence of HA-cumulus complex
450 disintegration as in the previous experiments. Finally, in the last experiment, ca. 50
451 microcarriers immobilized with HYAL-Psomes were put together with the cumulus cells,
452 resulting in disintegration of the cell cluster into small pieces after 30 min of incubation **(Figure**
453 **S9)** (more experiments with murine and bovine cumulus complex were added **in**
454 **Supplementary information**).

455 In this qualitative study, we can observe an interaction between immobilized HYAL-Psomes
456 on the microcarrier surface and HA-cumulus complex which can be used as local HA digestion
457 in future in vivo scenarios, but further studies still need to be carried out with oocytes and under
458 more realistic conditions, also considering the mechanical removal of cumulus cells by the
459 action of post-capacitation sperm tail beating.

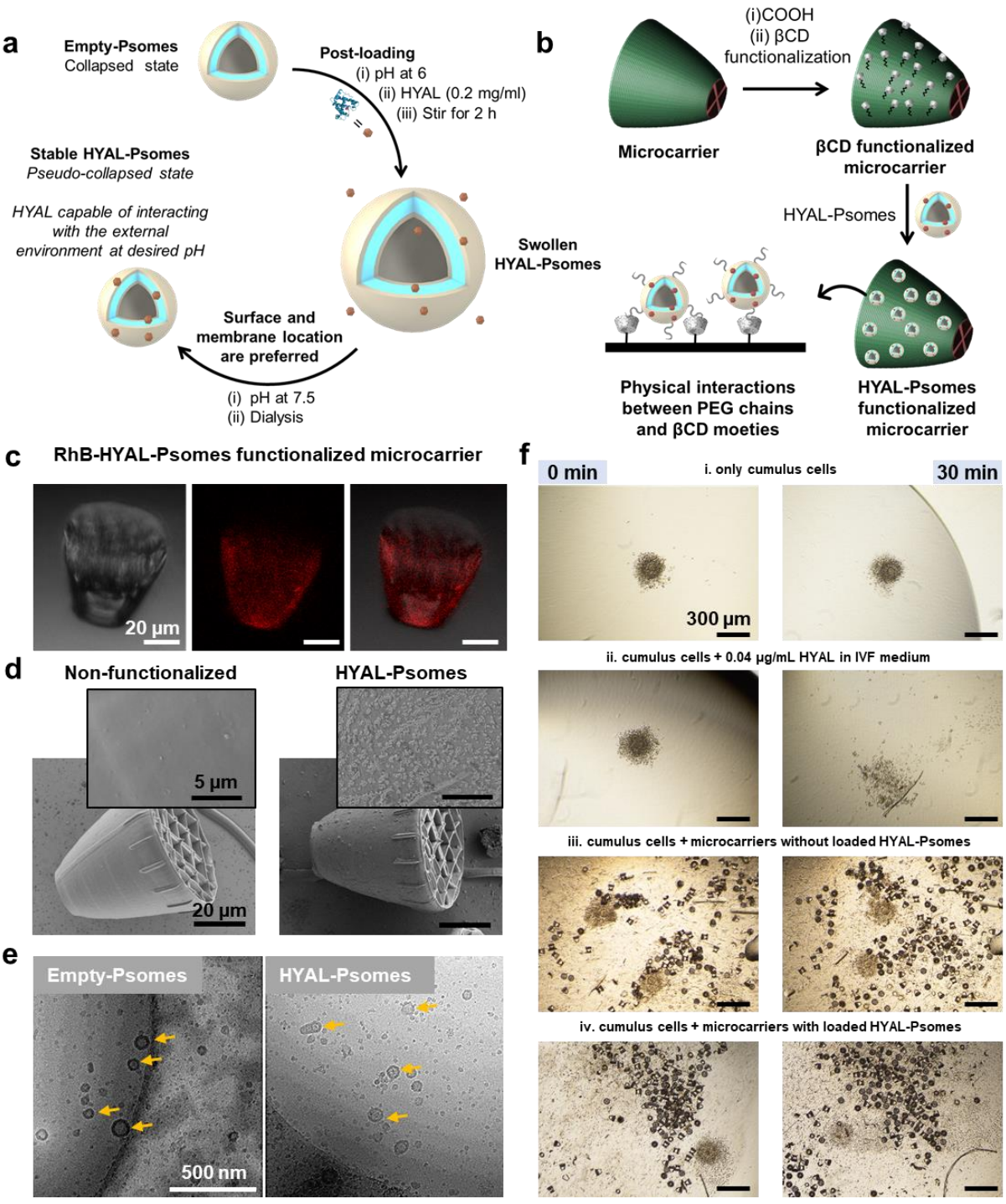

Figure 4. a) Schematic of the fabrication process of HYAL-Psomes, b) Schematic of the immobilization of HYAL-Psomes on the microcarrier surface for local degradation of HA-cumulus complex, c) CLSM characterization of immobilized microcarrier with RhB-HYAL-Psomes (in brightfield, fluorescence, and merged channel), d) SEM characterization of immobilized microcarrier with and without HYAL-Psomes, [the inset images show the respective surface in more detail], e) Cryo-TEM images of immobilized Empty-Psomes and HYAL-Psomes on the microcarrier surface (exemplary Psomes marked with yellow arrows), f) Qualitative study of the interaction of hyaluronidase with HA-cumulus

complex (with and without hyaluronidase in the solution and with and without HYAL-Psome loaded microcarriers).

2.4.3. Effect of HYAL and HYAL-Psomes on sperm motility

In **Figure S2c**, it is observed that sperm motility decreases in all conditions after 6h of incubation at 38°C. The decline of sperm motility in the case of pure sperm solution and sperm solution in presence of hyaluronidase (HYAL) was ca. 86%, and 75%, respectively. Likewise, sperm solution containing Empty-Psomes and HYAL-Psomes, showed a motility decrease of 90%, and 70%, respectively. In both cases, we could observe that sperm sample containing either HYAL solution or HYAL-Psomes, exhibited a higher motility rate than the samples without HYAL. This might be due to the fact that HYAL and other enzymes present in the sperm acrosome play an important role in the preparation of sperm prior oocyte fertilization. Hyaluronidases in particular are responsible of catalyzing the hyaluronic acid present in the cumulus complex.[65] In general, there is a complex cascade of reactions associated with changes in the composition of the sperm membrane during the sperm journey, some of them triggered by hyaluronidases, which has a direct influence on sperm motility. However further studies need to be realized to better understand the underlying mechanism and correlation between sperm motility, and a particular enzyme activity.

In addition, for a better understanding of the mutual effect of HYAL-Psomes and heparin on sperm motility, we performed combinatory experiments, involving both HYAL-Psomes and heparin, mimicking the envisioned in vivo scenario. In **Figure S2d**, sperm motility was measured in solution in presence of heparin with HYAL, heparin with Empty-Psomes, and heparin with HYAL-Psomes. As discussed in **Figure S2c**, the presence of HYAL in the solution had a positive effect on sperm motility. In **Figure S2d**, the same effect was observed for hyperactivated sperm cells when there was HYAL in the solution, the sperm motility was preserved significantly compared to the pure sperm solution (improvement of sperm motility ca. 40% for hyperactivated sperm cells in presence of HYAL, and ca. 66% for hyperactivated sperm cells in presence of HYAL-Psomes).

In the case of hyperactivated sperm cells in presence of polymersomes (Empty-Psomes and HYAL-Psomes), we observed better preservation of sperm motility. According to the previously reported work from Deng and coauthors, polymersomes can react with reactive oxygen species (ROS).[66,67] ROS are caused by oxidative stress that sperm experience during manipulation, reducing their motility. Therefore, and based on the obtained results,

polymersomes possibly react with oxygen species in the solution, removing them and preserving the motility of hyperactivated sperm cells for a longer time. As heparin and hyaluronidase activity affect the composition of the sperm head membrane differently, it is expected that sperm motility is also influenced, however the underlying physicochemical effects by the interplay of both heparin and hyaluronidase, as well as, of other enzymes present in the sperm acrosome, require deeper investigations.

2.5. Sperm-microcarrier motion performance in oviduct-mimicking fluids

As explained above, the microcarrier has ca. 16 available cavities for the coupling of sperm cells; however, due to possible tail beating interference, we observed coupling of up to 10 sperm cells in our experiments (an example of multiple sperm cells coupled into a microcarrier is shown in **Figure 5a**, with sperm coupling pointed out by the yellow arrow) **(Videos S5)**. In **Figure 5b**, the trajectories of the optimized sperm-microcarrier are shown in different media (SP-TALP, and SP-TALP enriched with 0.2% MC). The latter shows the same rheological behavior as the early luteal phase of bovine oviduct fluid BOF-EL (the phase after ovulation where fertilization takes place).[30] The mean velocity of 20 sperm-microcarriers showed 50% decrease in the measured velocity from SP-TALP to SP-TALP enriched with 0.2% MC, which agrees with previous results **(Figure 5c; Video S6 and Video S7)**.[30]

2.5.1. Capture, transport, and release of sperm cells

Another challenge which should be considered regarding the biomedical application of such microcarriers is their controllability. When motile sperm cells propel the synthetic microcarrier and push it forward, by applying external stimuli such as a non-invasive and biocompatible magnetic field, the carrier can be guided toward a desirable location. In this work, the incorporation of a thin film of iron was included for the magnetic actuation. An external magnetic field was used for the guidance of microcarriers which were propelled by motile sperm cells. After completion of sperm cell coupling into microcarriers, they were steered to the desired location. In all these experiments, a permanent neodymium magnet with a magnetic field flux of ca. 20 mT at the location of the sample was used **(Figure S10)**.

To demonstrate the whole process of capture, transport, and release of multiple motile sperm cells with microcarriers, a microfluidic system containing three reservoirs made of polydimethylsiloxane (PDMS) was used **(Figure 5d; detail in Supplementary information)**. Before the experiment, the microchannel and microcarriers were treated with Pluronic acid for

30 min, and washed with distilled water. Then the microcarriers were released from their substrate with a sufficient quantity of SP-TALP. Subsequently, sperm solution (swim-up process-selected sperm cells immersed in fresh SP-TALP) was added to the microchannel **(detail in Supplementary information)**. After sperm coupling, sperm-propelled microcarriers in the first reservoir were guided through the microchannel by means of an external magnetic field, reaching a second reservoir. Next, their orientation was altered by the external magnetic field to ultimately reach the third reservoir, where sperm release was demonstrated **(Figure 5d)**. During the whole transport, the temperature was fixed at 35°C using a Peltier element under the petri dish. After reaching the last reservoir, the temperature was increased to 40°C. The PNIPAM microgate opened to an appropriate size to enable sperm to be released one at a time **(Figure 5e)**. The whole process of capture, transport, guidance, and release of at least 5 sperm cells is shown in **Video S8.** Another example of the whole process can be seen in **Video S9**.

Furthermore, we analyzed the performance of the developed sperm-microcarriers on ex vivo fallopian tube tissue. For this experiment, we fabricated a double-layer parafilm channel (height ~ 1mm), in which we placed a flat piece of ex vivo oviduct tissue (laying down on the bottom surface), and filled the whole chamber with sperm medium (SP-TALP). Then we introduced a small drop containing sperm cells and microstructures. Once the structures were coupled and pushed forward by the sperm cells, we used an external magnetic field (ca. 20 mT at the location of the sample) to guide the sperm-microcarriers toward the tissue. We did two types of imaging, one employing an upright microscope (reflective microscope), where we could observe the moving sperm-microcarriers swimming on top and underneath the tissue. We confirm the presence of the sperm microcarriers by fluorescence microscopy. The second imaging was done with an inverted microscope, to see sperm-microcarriers swimming below the tissue, between the bottom glass substrate and the oviduct tissue, or by flipping the parafilm channel to see the ones on top of the tissue when the light from behind illuminates it. As shown with fluorescence microscopy, after a certain time, the microcarrier swimming on top of the tissue started to get stuck (**Video S10 and Video S11**). For that further investigations on surface functionalization and protein-repellent coatings need to be realized to ensure optimal performance when employing them in living organisms. For instance, Wu and coauthors reported the helical micropropeller that can penetrate the vitreous humor in the eye which was functionalized with a perfluorocarbon surface coating to minimize the interaction of the microrobots with tissues including collagen bundles.[68] In another work, Cabanach and coauthors proposed non-

immunogenic stealth zwitterionic microrobots that avoid detection and phagocytosis from macrophages.[69]

2.6. Microcarriers as enhanced contrast agents for photoacoustic imaging

Finally, as the microcarriers were also coated with a thin film of gold (20 nm of Au), they could absorb infrared (IR) light and convert it into acoustic waves, which is beneficial for their visualization using a dual ultrasound (US) and photoacoustic (PA) imaging system under scattering tissues for future in vivo applications. PA imaging provides the penetration depth of US and the molecular specificity of optics, and has successfully been implemented in in vivo imaging of micromotors.[70] The setup is equipped with a linear array of US transducer and fiber optic bundles on either side of the transducer for illumination (680 to 970 nm), as shown in **Figure 5f**.

To observe the dynamic behavior of the microcarriers in the imaging system, a transparent intravascular polyurethane (IPU) phantom tube was used **(Figure 5g; detail in Supplementary information)**. The dynamic imaging of a cluster of microcarriers is shown in time-lapse images from 0 to 2.80 s **(Figure 5h, i)**, comparing optical, US, and PA imaging modes. The dashed-circle shows the position of the cluster of microcarriers at starting position A and final position B after travel. The magnetic guidance was achieved using a hand-held permanent magnet placed close to the phantom tube. It was possible to image a cluster of microcarriers with absorbing metal layers coated on the surface. Such metal layers provided strong PA amplitude values as compared to the control (with no microcarriers) in comparable imaging regions **(Figure 5h, ii)**.

According to **Figure S11**, it is observed that the employed illumination during photoacoustic imaging is not sufficient to induce local heating (by photothermal effect) in the sperm microcarriers, which can undesirably cause a shape change in the microcarrier PNIPAM microgate **(detailed characterization and calculations are included in the Supplementary information)**.

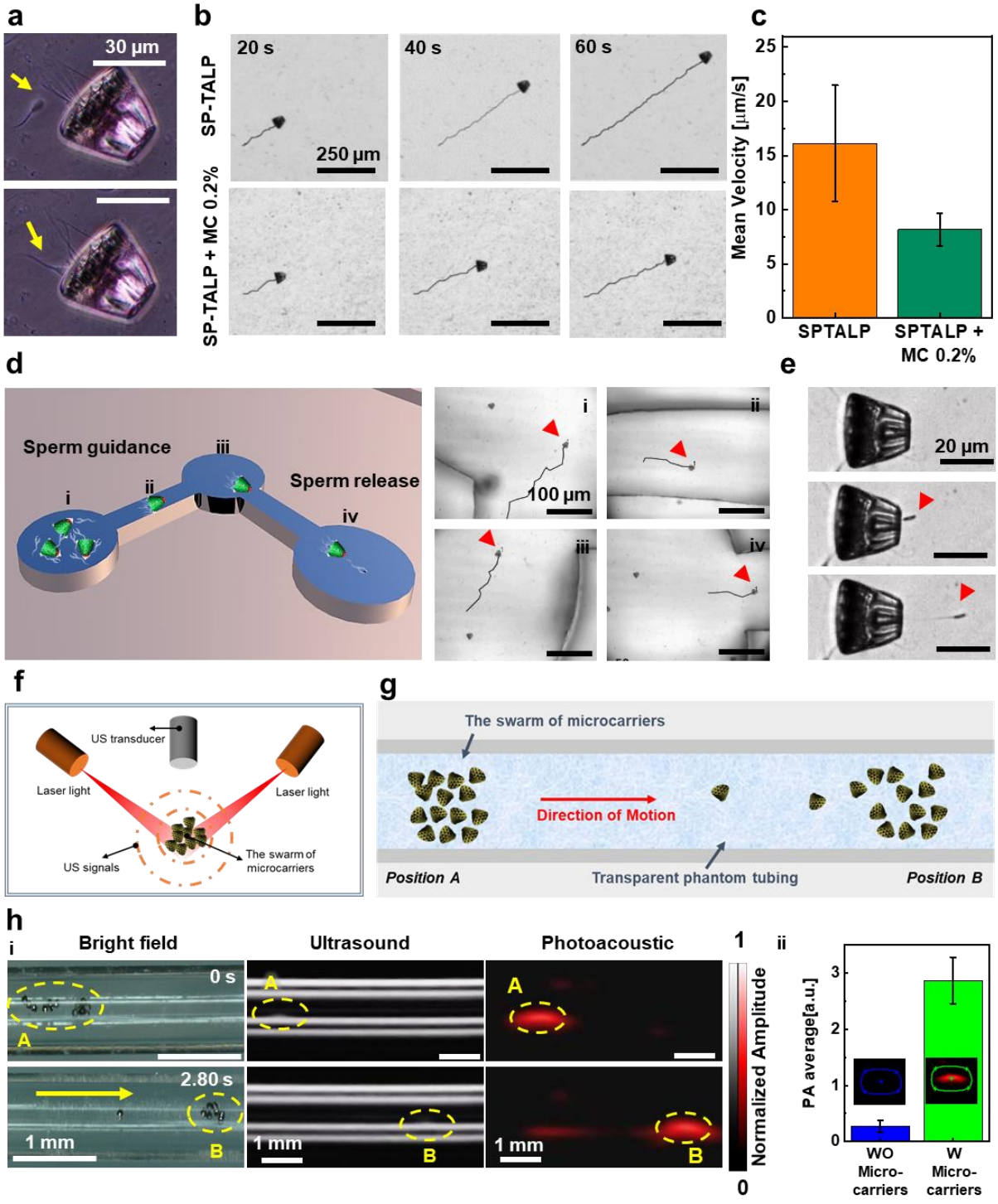

Figure 5. a) Sperm coupling into a microcarrier cavity, the yellow arrow shows the position of the sperm head, b) Sperm-microcarrier trajectory in the SP-TALP, and SP-TALP enriched with 0.2% of MC, c) The sperm mean velocity in SP-TALP and SP-TALP + 0.2% MC ($n_{microcarrier}$=20, N=3, mean, ±SD), d) Schematic of microfluidic channel to demonstrate sperm capture, guidance/transport, and release with the sequential figures (the red arrow shows sperm-microcarrier location), e) The sequential images of sperm release at physiologically relevant temperature ca. 39°C (the red arrow shows the position of the sperm head), f) Schematic showing the working principle of the employed hybrid US and PA imaging system, g) Schematic of a swarm of microcarriers in a phantom tube immersed in a water bath for real-

time tracking of their movement, h) (i) Time-lapse images of moving microcarriers in the bright field, US , and PA modes (yellow dashed-circle shows the cluster of moving microcarriers at starting position A and final position B), (ii) PA amplitude values extracted from the captured PA images of moving microcarriers, compared to the control sample (the tube with no microcarriers) (n=2, N=3, mean, ±SD).

3. Conclusion and Outlook

In the current work we focused on assisting sperm cells when sperm count is very low (also called oligospermia) in order to increase the chances of oocyte fertilization in vivo. For this reason, we fabricated multifunctional sperm-hybrid microcarriers able to assist a limited number of sperm cells. First by realizing the in-situ sperm capacitation/hyperactivation by the local release of heparin. Second by triggering the sperm release on the desired location, and finally by facilitating the removal of the cumulus complex that surrounds the oocyte to open a path for the sperm cells to reach the oocyte zona pellucida.

For that purpose, a stream-lined microstructure with a stimuli-responsive “microgate” was fabricated. The microgate was loaded with heparin prior sperm capture. The optimum concentration of heparin per microcarrier was calculated and the effect of the heparin on sperm hyperactivation was also investigated. We confirmed that temperature in combination with heparin has a significant effect on sperm hyperactivation as both increase sperm metabolism and affect their motion performance.

Additionally, the microcarriers were functionalized with surface-active hyaluronidase-loaded polymersomes, which enable a high loading efficiency while preserving their enzymatic activity. We demonstrate that the enzyme was stably loaded onto the polymersomes under varying pH, allowing for local enzymatic reactions and facilitating the digestion of the extracellular matrix of the cumulus cells via hyaluronic acid surrounding the oocyte.

We also show that such microcarriers containing ca. 10 sperm cells can be steered in a targeted fashion by means of an external magnetic field, which was demonstrated in a confined microfluidic channel using an artificial oviduct fluid. We successfully report the capture, transport, and release of multiple sperm cells by the designed microcarriers. The microstructures were coated with Au, enabling preliminary bioimaging tests to be conducted using photoacoustic imaging. The microstructures’ photoacoustic signal was obtained by employing phantom plastic tubes while moving, demonstrating a possibility to track them under scattering tissues for future in vivo applications.

Despite these important achievements, compared to previously reported single-sperm carriers, there are still many challenges to be addressed before the microcarriers can be applied in vivo. For example, these microcarriers were designed and proved using bovine sperm. However, in order to perform animal trials, and due to the current limitations of imaging techniques in terms of spatiotemporal resolution and penetration depth, small animal models (e.g., mice) are preferable for establishing the technology, and for that reason will be considered in the future.

The coupling and transport of multiple microcarriers, where each contains up to 10 sperm cells, might be sufficient to demonstrate oocyte fertilization, but their cooperative action require further optimization. Also, the interactions of such a microcarrier with the surrounding tissue remains to be studied. We have so far evaluated their performance in artificial oviduct fluids with similar rheological properties, but the interaction with the oviduct epithelial and ciliary cells is the aim of future studies by our group; before initiating animal trials, the 3Rs principle (reduction, refining, and recycling) should be followed and supported by a complete set of experiments performed in vitro and with ex vivo tissue.[71] Furthermore, these structures should ideally be biodegradable. There are biodegradable photoresists and reported protocols for employing photo-patternable gelatin currently available, which might be used in place of IPS photoresist.[72,73] Gelatin is also responsive to pH and temperature changes, and current efforts are being made to develop biodegradable stimuli-responsive hydrogels.[54,74,75]

All in all, we have addressed several challenges reported in the literature: namely, the transport of multiple sperm cells, their imaging for future in vivo applications, and the addition of multiple functions (sperm capacitation and cumulus cell removal). To accomplish these aims, we employed different functional materials to fabricate microcarriers with adaptable stimuli-responsive microgates for different operations. Such stimuli are already present in the fallopian tube, which will circumvent the need for external triggering in future in vivo experiments. This advanced 4D-printed multifunctional microcarrier made with two-photon lithography, offers a plethora of possibilities not only in the field of microrobotics-assisted therapy and diagnosis but also for on-chip applications.

Acknowledgements

Authors thank Ms. Franziska Hebenstreit for conducting the cell culture experiment and bringing bovine ovary from slaughterhouse along with Mr. Friedrich Striggow to collect cumulus cells, Ronald Naumann, from MPI-CBG for providing the murine gametes samples, Mr. Lukas Schwarz and Mr. Haifeng Xu for the initial support on the microcarrier design. Mr.

Friedrich Striggow and Dr. Sandhya Rani Goudu for conducting internal revision of the paper, Ms. Franzisca Kucharczyk for performing the fluorescence spectroscopy, Mr. Yang Zhou for performing Cryo-TEM, and Mr. Michael Göbel for preparing SEM images.

Funding

This work is part of the projects that have received funding from the European Research Council (ERC) under the European Union's Horizon 2020 research and innovation program (grant agreement nos. 835268 and 853609). This work was supported by the German Research Foundation DFG (Gottfried Wilhelm Leibniz Prize granted in 2018, SCHM 1298/22-1 and KA5051/1-1).

References

[1] B. E.-F. de Ávila, P. Angsantikul, J. Li, M. Angel Lopez-Ramirez, D. E. Ramírez-Herrera, S. Thamphiwatana, C. Chen, J. Delezuk, R. Samakapiruk, V. Ramez, L. Zhang, J. Wang, *Nat. Commun.* **2017**, *8*, 1.

[2] O. Felfoul, M. Mohammadi, S. Taherkhani, D. de Lanauze, Y. Zhong Xu, D. Loghin, S. Essa, S. Jancik, D. Houle, M. Lafleur, L. Gaboury, M. Tabrizian, N. Kaou, M. Atkin, T. Vuong, G. Batist, N. Beauchemin, D. Radzioch, S. Martel, *Nat. Nanotechnol.* **2016**, *11*, 941.

[3] S. K. Srivastava, G. Clergeaud, T. L. Andresen, A. Boisen, *Adv. Drug Deliv. Rev.* **2019**, *1*, 41.

[4] A. Aziz, S. Pane, V. Iacovacci, N. Koukourakis, J. Czarske, A. Menciassi, M. Medina-Sánchez, O. G. Schmidt, *ACS Nano* **2020**, *14*, 10865.

[5] Z. Wu, L. Li, Y. Yang, P. Hu, Y. Li, S.-Y. Yang, L. V. Wang, W. Gao, *Sci. Robot.* **2019**, *4*, DOI 10.1126/scirobotics.aax0613.

[6] A. Servant, F. Qiu, M. Mazza, K. Kostarelos, B. J. Nelson, *Adv. Mater.* **2015**, *27*, 2981.

[7] M. Medina-Sánchez, O. G. Schmidt, *Nature* **2017**, *545*, 406.

[8] S. Martel, *Biomed. Microdevices* **2012**, *14*, 1033.

[9] O. Yasa, P. Erkoc, Y. Alapan, M. Sitti, *Adv. Mater.* **2018**, *30*, 1804130.

[10] J. Zhuang, M. Sitti, *Sci. Rep.* **2016**, *6*, 32135.

[11] J. Han, J. Zhen, V. Du Nguyen, G. Go, Y. Choi, S. Y. Ko, J.-O. Park, S. Park, *Sci. Rep.* **2016**, *6*, 28717.

[12] D. Akin, J. Sturgis, K. Ragheb, D. Sherman, K. Burkholder, J. P. Robinson, A. K. Bhunia, S. Mohammed, R. Bashir, *Nat. Nanotechnol.* **2007**, *2*, 441.

[13] S. Taherkhani, M. Mohammadi, J. Daoud, S. Martel, M. Tabrizian, *ACS Nano* **2014**, *8*, 5049.

[14] S. Martel, C. C. Tremblay, S. Ngakeng, G. Langlois, *Appl. Phys. Lett.* **2006**, *89*, 233904.

[15] R. Di Leonardo, L. Angelani, D. Dell'Arciprete, G. Ruocco, V. Iebba, S. Schippa, M. P. Conte, F. Mecarini, F. De Angelis, E. Di Fabrizio, *Proc. Natl. Acad. Sci.* **2010**, *107*, 9541.

[16] N. Darnton, L. Turner, K. Breuer, H. C. Berg, *Biophys. J.* **2004**, *86*, 1863.

[17] C. K. Schmidt, M. Medina-Sánchez, R. J. Edmondson, O. G. Schmidt, *Nat. Commun.* **2020**, *11*, 5618.

[18] V. Magdanz, M. Medina-Sánchez, L. Schwarz, H. Xu, J. Elgeti, O. G. Schmidt, *Adv. Mater.* **2017**, *29*, 1606301.

[19] L. Schwarz, M. Medina-Sánchez, O. G. Schmidt, *Reproduction* **2020**, *159*, R83.

[20] M. Eisenbach, *Rev. Reprod.* **1999**, *4*, 56.

[21] A. Bahat, M. Eisenbach, *Mol. Cell. Endocrinol.* **2006**, *252*, 115.

[22] V. Kantsler, J. Dunkel, R. E. Goldstein, *Biophys. J.* **2014**, *106*, 210a.

[23] D. Woolley, *Reproduction* **2003**, *126*, 259.

[24] M. Medina-Sánchez, H. Xu, O. G. Schmidt, *Ther. Deliv.* **2018**, *9*, 303.

[25] V. Kantsler, J. Dunkel, M. Blayney, R. E. Goldstein, *Elife* **2014**, *3*, e02403.

[26] Z. Zhang, J. Liu, J. Meriano, C. Ru, S. Xie, J. Luo, Y. Sun, *Sci. Rep.* **2016**, *6*, 23553.

[27] M. Medina-Sánchez, L. Schwarz, A. K. Meyer, F. Hebenstreit, O. G. Schmidt, *Nano Lett.* **2016**, *16*, 555.

[28] V. Magdanz, S. Sanchez, O. G. Schmidt, *Adv. Mater.* **2013**, *25*, 6581.

[29] V. Magdanz, M. Medina-Sánchez, Y. Chen, M. Guix, O. G. Schmidt, *Adv. Funct. Mater.* **2015**, *25*, 2763.

[30] F. Striggow, M. Medina-Sánchez, G. K. Auernhammer, V. Magdanz, B. M. Friedrich, O. G. Schmidt, *Small* **2020**, *16*, 2000213.

[31] V. Magdanz, M. Guix, F. Hebenstreit, O. G. Schmidt, *Adv. Mater.* **2016**, *28*, 4084.

[32] H. Xu, M. Medina-Sánchez, V. Magdanz, L. Schwarz, F. Hebenstreit, O. G. Schmidt, *ACS Nano* **2018**, *12*, 327.

[33] V. Magdanz, I. S. M. Khalil, J. Simmchen, G. P. Furtado, S. Mohanty, J. Gebauer, H. Xu, A. Klingner, A. Aziz, M. Medina-Sánchez, O. G. Schmidt, S. Misra, *Sci. Adv.* **2020**, *6*, eaba5855.

[34] S. Bartnitzky, V. Blumenauer, U. Czeromin, D. Fehr, C. Gnoth, C. Grewe, J. Kru, M. Kupka, A. Tandler-Schneider, *D·I·R Annual 2020-The German IVF-Registry*, **2021**.

[35] F. Rajabasadi, L. Schwarz, M. Medina-Sánchez, O. G. Schmidt, *Prog. Mater. Sci.* **2021**, *120*, 100808.

[36] M. Wei, Y. Gao, X. Li, M. J. Serpe, *Polym. Chem.* **2017**, *8*, 127.

[37] D. Han, Z. Lu, S. A. Chester, H. Lee, *Sci. Rep.* **2018**, *8*, 1963.

[38] Y. Okada, F. Tanaka, *Macromolecules* **2005**, *38*, 4465.

[39] L. D. Zarzar, P. Kim, M. Kolle, C. J. Brinker, J. Aizenberg, B. Kaehr, *Angew. Chemie* **2011**, *123*, 9528.

[40] A. Nishiguchi, A. Mourran, H. Zhang, M. Möller, *Adv. Sci.* **2018**, *5*, 1700038.

[41] A. Tudor, C. Delaney, H. Zhang, A. J. Thompson, V. F. Curto, G.-Z. Yang, M. J. Higgins, D. Diamond, L. Florea, *Mater. Today* **2018**, *21*, 807.

[42] M. Ergüven, T. İrez, *Fertil. Steril.* **2020**, *114*, e352.

[43] A. Kaul, W. D. Short, X. Wang, S. G. Keswani, *Int. J. Mol. Sci.* **2021**, *22*, 3204.

[44] M. Hippler, E. Blasco, J. Qu, M. Tanaka, C. Barner-Kowollik, M. Wegener, M. Bastmeyer, *Nat. Commun.* **2019**, *10*, 232.

[45] J. Van Duijn, C., *Mikroskopie* **1960**, *14*, 265.

[46] H. Xu, M. Medina-Sánchez, M. F. Maitz, C. Werner, O. G. Schmidt, *ACS Nano* **2020**, *14*, 2982.

[47] H. Xu, M. Medina-Sánchez, W. Zhang, M. P. H. Seaton, D. R. Brison, R. J. Edmondson, S. S. Taylor, L. Nelson, K. Zeng, S. Bagley, C. Ribeiro, L. P. Restrepo, E. Lucena, C. K. Schmidt, O. G. Schmidt, *Nanoscale* **2020**, *12*, 20467.

[48] H.-W. Su, Y.-C. Yi, T.-Y. Wei, T.-C. Chang, C.-M. Cheng, *Bioeng. Transl. Med.* **2017**, *2*, 238.

[49] B. H. Tan, R. H. Pelton, K. C. Tam, *Polymer (Guildf).* **2010**, *51*, 3238.

[50] S. S. Suarez, *Hum. Reprod. Update* **2008**, *14*, 647.

[51] S. Suarez, H.-C. Ho, *Reprod. Domest. Anim.* **2003**, *38*, 119.

[52] J. Stewart-Savage, *Biol. Reprod.* **1993**, *49*, 74.

[53] K. Bedu-Addo, L. Lefièvre, F. L. C. Moseley, C. L. R. Barratt, S. J. Publicover, *MHR Basic Sci. Reprod. Med.* **2005**, *11*, 683.

[54] C. Ridzewski, M. Li, B. Dong, V. Magdanz, *ACS Appl. Bio Mater.* **2020**, *3*, 1616.

[55] R. Rikmenspoel, *J. Exp. Biol.* **1984**, *108*, 205.

[56] M. Abdul-Aziz, J. Meriano, R. F. Casper, *Fertil. Steril.* **1996**, *65*, 977.

[57] F. Meng, Z. Zhong, J. Feijen, *Biomacromolecules* **2009**, *10*, 197.

[58] J. Gaitzsch, D. Appelhans, L. Wang, G. Battaglia, B. Voit, *Angew. Chemie Int. Ed.* **2012**, *51*, 4448.

[59] R. Ccorahua, S. Moreno, H. Gumz, K. Sahre, B. Voit, D. Appelhans, *RSC Adv.* **2018**, *8*, 25436.

[60] H. Gumz, S. Boye, B. Iyisan, V. Krönert, P. Formanek, B. Voit, A. Lederer, D. Appelhans, *Adv. Sci.* **2019**, *6*, 1801299.

[61] E. Geervliet, S. Moreno, L. Baiamonte, R. Booijink, S. Boye, P. Wang, B. Voit, A. Lederer, D. Appelhans, R. Bansal, *J. Control. Release* **2021**, *332*, 594.

[62] S. Hugentobler, D. . Morris, M. . Kane, J. . Sreenan, *Theriogenology* **2004**, *61*, 1419.

[63] K. Y. B. Ng, R. Mingels, H. Morgan, N. Macklon, Y. Cheong, *Hum. Reprod. Update* **2018**, *24*, 15.

[64] B. R. L. de Moura, M. C. A. Gurgel, S. P. Machado, P. A. Marques, J. R. Rolim, M. C. de Lima, L. L. Salgueiro, *JBRA Assist. Reprod.* **2017**, *21*, 27.

[65] Y. Lin, K. Mahan, W. F. Lathrop, D. G. Myles, P. Primakoff, *J. Cell Biol.* **1994**, *125*, 1157.

[66] Y. Deng, H. Chen, X. Tao, F. Cao, S. Trépout, J. Ling, M.-H. Li, *Biomacromolecules* **2019**, *20*, 3435.

[67] K. Nowicka-Bauer, B. Nixon, *Antioxidants* **2020**, *9*, 134.

[68] Z. Wu, J. Troll, H.-H. Jeong, Q. Wei, M. Stang, F. Ziemssen, Z. Wang, M. Dong, S. Schnichels, T. Qiu, P. Fischer, *Sci. Adv.* **2018**, *4*, eaat4388.

[69] P. Cabanach, A. Pena-Francesch, D. Sheehan, U. Bozuyuk, O. Yasa, S. Borros, M. Sitti, *Adv. Mater.* **2020**, *32*, 2003013.

[70] A. Aziz, J. Holthof, S. Meyer, O. G. Schmidt, M. Medina-Sánchez, *Adv. Healthc. Mater.* **2021**, *10*, 2101077.

[71] S. Ihle, *Animal Experimentation in Research: The 3Rs Principle and the Validity of Scientific Research*, Life Sciences, **2019**.

[72] X. Hu, I. C. Yasa, Z. Ren, S. R. Goudu, H. Ceylan, W. Hu, M. Sitti, *Sci. Adv.* **2021**, *7*, DOI 10.1126/sciadv.abe8436.

[73] S. R. Goudu, I. C. Yasa, X. Hu, H. Ceylan, W. Hu, M. Sitti, *Adv. Funct. Mater.* **2020**, *30*, 2004975.

[74] Z. Wu, X. Lin, X. Zou, J. Sun, Q. He, *ACS Appl. Mater. Interfaces* **2015**, *7*, 250.

[75] M. Dong, X. Wang, X. Chen, F. Mushtaq, S. Deng, C. Zhu, H. Torlakcik, A. Terzopoulou, X. Qin, X. Xiao, J. Puigmartí-Luis, H. Choi, A. P. Pêgo, Q. Shen, B. J. Nelson, S. Pané, *Adv. Funct. Mater.* **2020**, *30*, 1910323.

Table of Content

4D printed microcarriers are developed to perform various functions, including multiple sperm cargo-release, local sperm capacitation and mediation of cumulus oocyte complex removal by in-situ enzymatic reactions.

Fatemeh Rajabasadi, Silvia Moreno, Kristin Fichna, Azaam Aziz, Dietmar Appelhans, Oliver G. Schmidt, and Mariana Medina-Sánchez**

Multifunctional 4D-printed sperm-hybrid microcarriers for assisted reproduction

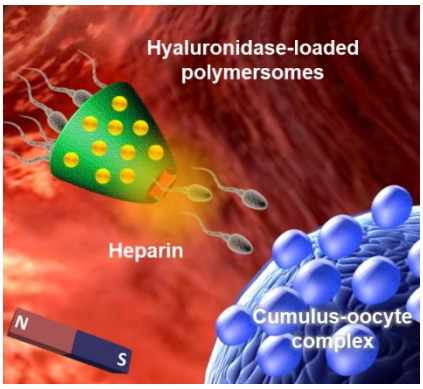

Supporting Information

Multifunctional 4D-printed sperm-hybrid microcarriers for assisted reproduction

Fatemeh Rajabasadi, Silvia Moreno, Kristin Fichna, Azaam Aziz, Dietmar Appelhans, Oliver G. Schmidt, and Mariana Medina-Sánchez**

1. Experimental section

Synthesis of PNIPAM

The resist was prepared dissolving 400 mg N-isopropylacrylamide (Sigma-Aldrich), 40 mg N,N′-methylenebis(acrylamide) (Sigma-Aldrich), and 15 mg lithium phenyl(2,4,6-trimethylbenzoyl)phosphinate (Sigma-Aldrich), in 460 µL of ethylene glycol (Sigma-Aldrich). Afterward, 5 mg of acryloxyethyl thiocarbamoyl Rhodamine B (Polysciences) was added for optical characterization purpose.

Fabrication of microcarrier

The fabrication of microcarrier is consisted of two consecutive steps. First, the rigid body of whole microcarriers are 3D printed with IPS photoresist through the oil immersion configuration of DLW (25x objective, NA = 0.8). Then microstructures were immersed in mrDev 600 (micro resist technology GmbH) for 20 min followed by washing for 3 min in isopropanol. The sample was then dried using critical point drying (EM CPD300, Leica) and prepared for next writing step. In the second writing step, PNIPAM was drop casted onto the dried substrate and followed by two photon polymerization process. The PNIPAM part are written inside each pre-printed microcarrier. After developing sample in acetone and letting dried, to enable magnetic guidance, thin layers of 5 nm Ti, 15 nm Fe were deposited at an angle of 45° using electron beam deposition (Plassys). Finally, the structures were kept in water for further temperature test and storage (**Figure 1a,** main text).

Sperm coupling and optimization of the microcarrier geometry

The current design of the microcarrier was obtained experimentally through optimization of different geometries. We started with a very simple design, a cylinder (Figure S1, i), for a single sperm cargo-release. Then, we changed the cylindrical cap design to a stream-lined cap to prevent unwanted sperm escape from the large opening (Figure S1, ii). Afterward, we made a larger stream-lined microcarrier (ca. 50 µm long and 50 µm wide) (Figure S1, iii), not only to

carry multiple motile sperm cells with higher propulsion power but also to be close to the bioimaging spatial resolution range considering their use in future animal experiments. However, the coupling of sperm cells into the larger microcarriers was a bit random. Therefore, we added a grid into the design (Figure S1, iv), with individual cavities which lead to a more deterministic sperm coupling which also improved the sperm-microcarrier performance. Still as highlighted by the reviewer, not all 16 cavities were occupied by sperm cells, which can be associated to different factors: (i) the coupling of sperm to the microstructure occurs randomly and at different times, and (ii) the tail beating of the already coupled sperm cells create local flow streams which interfere with the coupling of new coming sperm cells (this effect is being more prominent when the number of coupled sperms increases). From our experiments, we have found that in most cases up to 10 sperm cells are coupled to the current microstructure design.

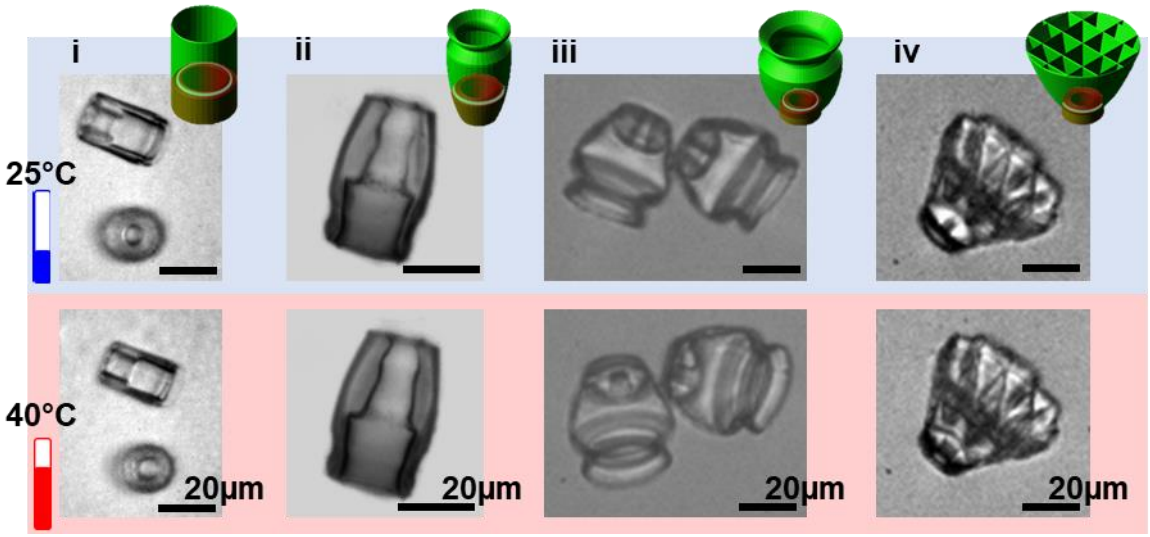

Figure S1. Investigation of different 4D-printed designs containing IPS body and PNIPAM gate for sperm carrying and their temperature response at cooling state 25°C and heating state 40°C with (i) cylindrical, (ii) stream-lined shape, (iii) larger stream-lined shape, and grid stream-lined cap design.

Preparation of sperm medium and sperm solution

Sperm medium: SP-TALP was prepared by dissolving 60 mg of BSA in 9.5 mL TL-Sperm and adding 0.5 mL Sodium Pyruvate and 20 µL Gentamycin sulfate. The solution was then sterile-filtered (modified Tyrode's Albumin-Lactate-Pyruvate Medium, CaissonLabs).

Sperm cell solution: The cryopreserved bovine semen straws (kindly provided by Masterrind GmbH) were withdrawn from the liquid nitrogen storage tank, thawed for 5 min in the incubator

at 38°C and diluted in 2 mL SP-TALP medium. Then as a washing step to separate high speed and alive sperm cell the sample were centrifuged at 300 g for 5 min. After centrifuge the supernatant including dead/low motile sperm cell, remaining semen fluid was removed and the pellet of hyperactivated sperm cell was resuspended in 2 mL fresh SP-TALP.

Microfluidic channels

Parafilm chip: It is included two microscope cover slips (24 × 60 mm, VWR) were washed in acetone and isopropanol. Thin strips of parafilm consisted two layers of thin strips of parafilm were sandwiched with two coverslips by placing them on hotplate, heating up to 120°C and gently pressing the two coverslips together. This resulted in channels with an area of 26 × 26 mm, a height of 150 µm and openings on both ends.

PDMS microchannel: PDMS gel was prepared with the base monomer and curing agent at a ratio of 10:1. After 30 min of degassing inside desiccator, the mixture was plasticized at 75°C for 3 h. After that, the polymerized PDMS was peeled off and punched into corresponding inlets and outlets. Finally, the PDMS channel and a glass slide substrate were treated in O_2 plasma for 1 min and then bound together by heating at 90°C for 20 min.

For the capture, transport and release experiment we used a PDMS microchannel contains three reservoirs with ($\varphi = 2$ mm) connected through narrow channels (length = 5 mm, width = 200 µm, height = 300 µm) (**Figure 5d**, main text).

MTS-Assay

MTS-assay as a quantitative colorimetric method uses for rapid, sensitive and accurate measurement of viable cells in a proliferation assay (MTS Assay Kit, abcam, ab197010). For this purpose, Madin Darby Canine Kidney (MDCK) cells (ca. 5000 cells per each well) are cultured in a 96-well microtiter plate in a final volume of 200 µL per each well (48 h of incubation, in dark, 38°C). Then 20 µL per well MTS Reagent is added into each well and incubated for 2 h at 38°C in standard culture conditions. For the absorbance measurement, first the plate is shacked slightly and the absorbance is measured at OD=490 nm.

Temperature actuation test of PNIPAM and video recording

The thermal actuation tests were carried out under the same conditions while using a Peltier element for heating and cooling the sample to the desired temperature and the videos were

recorded with a Phantom Miro eX2 high-speed camera from VisionResearch mounted onto a reflective microscope (Zeiss, 20x objective).

In situ preparation of microcarriers and sperm cells

In this work we used bovine spermatozoa (Cryopreserved bovine sperm cells, Masterrind GmbH, Meißen, Germany). To operate investigation of interaction between bovine sperm cells and microcarriers, first 5 µL sperm medium (SP-TALP) is drop casted on the substrate and peeled off microcarriers with the pipet tip and subsequently squeezed them into the pipet. Then the microcarriers are injected to the microfluidic channel and afterward sperm solution consisted of bovine sperm cells in SP-TALP was added to the chip. Before adding microcarriers and sperm cell solution into the chip, microfluidic channel and microcarriers are submerged in Pluronic acid for 30 min (dissolved 100 µg of Pluronic F-127 in 100 mL distilled water 10-4% $\frac{w}{v}$), and washed 3 times with SP-TALP to remove extra solutions. Pluronic acid is a nonionic surfactant that is 100% active and relatively non-toxic to cells at low concentration. Pluronic sample treatment can be increased the water solubility of hydrophobic surfaces or otherwise it can be enhanced the miscibility of two substances with different hydrophobicity. Because of the cell cushioning effect of Pluronic acid, it can be reduced stressful shear condition between sperm cells and microcarriers during coupling. Subsequently, motile sperm cells selected by pellet swim up were added into the microfluidic channel where the microcarriers are injected.

Loading of microcarriers with heparin

The microcarriers (1500 structure in 100 µL) were incubated in 0.1 mg mL^{-1} heparin-fluorescent conjugate in TALP (sperm medium without BSA), at room temperature (lower than LCST, expanded state of PNIPAM) for 2 h. Then washed two times with fresh TALP to remove extra solutions.

All the sperm velocities were analyzed by computer-assisted sperm analysis (CASA, AndroVision®, Minitub GmbH, Germany) for at least 200 sperm cells per each condition and triplicate replications.

Toluidine blue assay

For a quantitative analysis, calculating heparin amount per each microcarrier, toluidine blue assay was carried out. For the assay, first heparin-loaded microcarriers were suspended in fresh SP-TALP. Then it shacked gently for 10 min to dispersed homogenously the microcarriers in

the solution. Afterward, the solution containing microcarriers were transferred to 96 well plate (triple measurement, 1500 microcarrier per each well) with 1:1 ratio of 0.1 mg mL^{-1} toluidine blue O-Solution in SP-TALP and the absorbance was measured at 631 nm. To see release rate, the ambient temperature of Multimode Plate Reader SpectraMax® were increased step by step. In each step after 1 min the absorbance measured at 631 nm.

Motility study of sperm cells

The motility of sperm cells was analyzed by computer-assisted sperm analysis (CASA, AndroVision®, Minitub GmbH, Germany) for at least 200 sperm cells per each condition and triplicate replications.

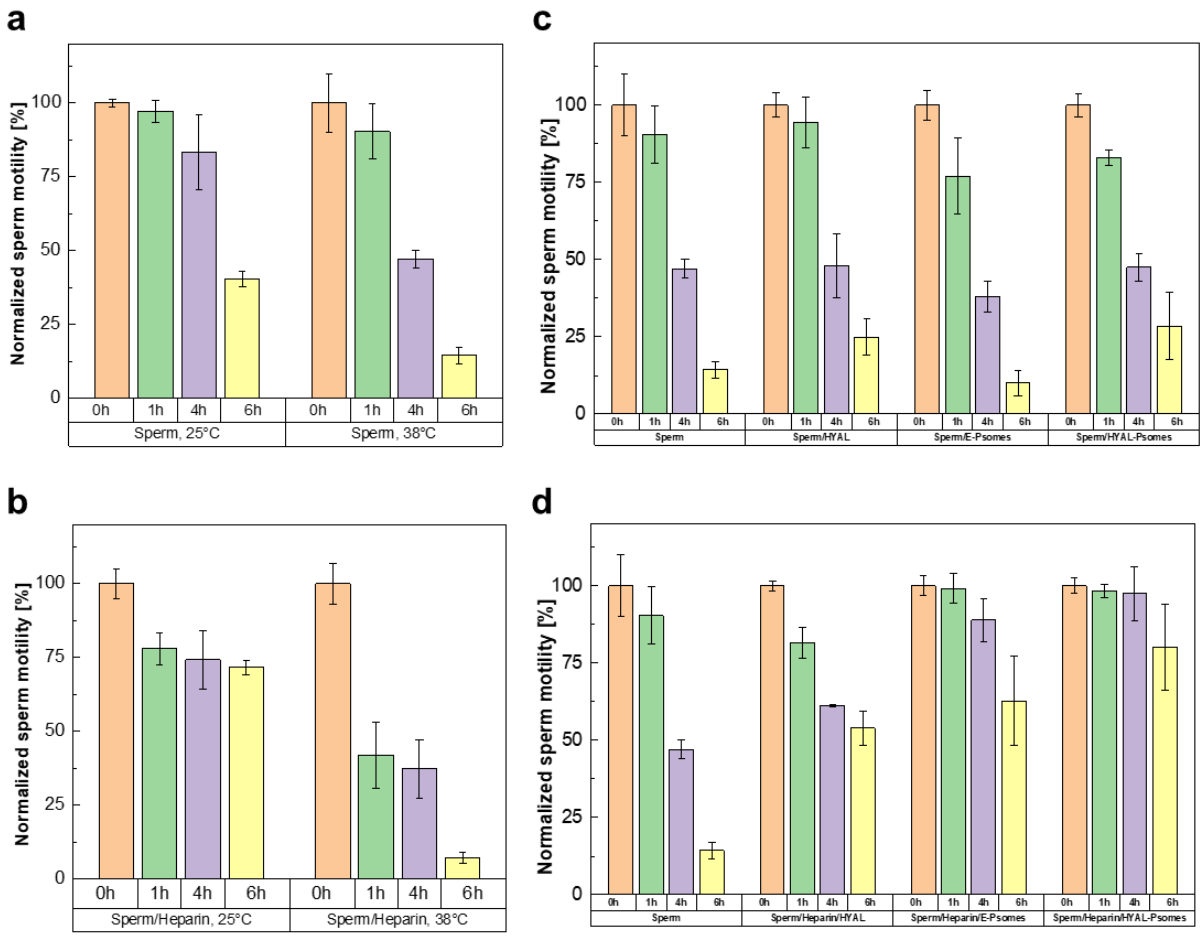

Figure S2. Investigation of the sperm motility a) At room temperature (25°C) and physiological temperature (38°C), after 0, 1, 4, and 6 H of incubation, b) In the presence of 0.1 mg/mL of heparin in the solution, c) In only sperm solution, sperm in 0.2 µg/mL of HYAL, sperm in 0.5 µg/mL of Empty Psomes (E-Psomes), sperm in dialyzed HYAL-Psomes (CHYAL< 0.2 µg/mL, CPsomes = 0.5 µg/mL), and d) In pure sperm solution, sperm in (0.1 mg/mL of heparin and 0.2 µg/mL of HYAL), sperm in (0.1

mg/mL of heparin and 0.5 µg/mL of E-Psomes), sperm in (0.1 mg/mL of heparin and dialyzed HYAL-Psomes (CHYAL< 0.2 µg/mL, CPsomes = 0.5 µg/mL). The motility rate was calculated by computer-assisted sperm analysis (CASA) (n=200, N=3, mean, ±SD). All motilities were normalized with the motility percentage at time 0 per each evaluated group.

Synthesis and characterization of block copolymers:

Amphiphilic block copolymers $mPEG_{45}$-b-P(DEAEMA-co-DMIBMA) (BCP) were successfully synthesized by atom transfer radical polymerization (ATRP).[1], [2] This block copolymer feature a methoxy end group at the hydrophilic poly(ethylene glycol) (PEG) segment, while the hydrophobic part consists of pH-sensitive 2-(diethylamino)ethyl methacrylate (DEAEM) and photo-crosslinker, 3,4-dimethyl maleic imidobutyl methacrylate (DMIBMA). The composition, molar mass and dispersity were well characterized by ^{1}H nuclear magnetic resonance spectroscopy (NMR) and size exclusion chromatography (SEC) **(Table S1)**.

Table S1. The composition, molecular weight and polydispersity index 'PDI' of the BCPs.

	DEAEMA amount	Crosslinker amount	PEG amount	Block ratio	M^1 [g mol^{-1}]	Mw^2 [g mol^{-1}]	Mn^2 [g mol^{-1}]	PDI
CE 875-7	81	23	45	1:2.3	23257	45500	38650	1.18
CE 880-1	63	22	45	1:1.9	19657	30800	36550	1.19

Fabrication and characterization of Empty-Psomes and HYAL-Psomes

Materials: Poly(ethylene glycol) methyl ether (MeO-PEG-OH; Mn = 2000 g mol^{-1}; $\frac{Mw}{Mn}$ = 1.05), 2,2´-bipyridine, 4-aminobutanol, 2-(diethylamino)ethyl methacrylate (DEAEMA), methacryloylic chloride, Rhodamine B isothiocyanate (RBITC), copper-I-bromide, aluminum oxide (neutral, activated), 4-amino-1-butanol (98 %), phosphate buffered saline (tablet), sodium hydroxide, Hyaluronic acid from Streptococcus equi, Hyaluronidase from bovine testes (Sigma-Aldrich), ethyl acetate, chloroform-d and dimethyl sulfoxide (DMSO) (Acros Organics), n-Hexane, hydrochloric acid (37%) and silica gel (Merck), Anhydrous 2-butanone (Fluka), triethylamine (Fluka) and anhydrous tetrahydrofuran (THF) (Sigma-Aldrich) [stored over a molecular sieve], Dialysis membrane Spectra/Por® Float-A-Lyzer® (CE MWCO 20 kDa and 300 kDa) (Carl Roth).

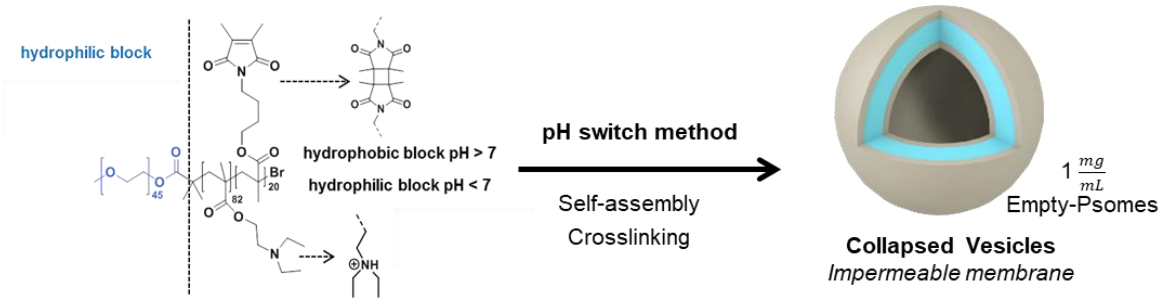

Figure S3. Formation of pH-responsive and photo-crosslinked Polymersomes (Empty-Psomes) as nanocarriers for HYAL.

Empty-Psomes were fabricated by the self-assembly of BCP using the so-called pH switch method.[1], [2] A solution of 1 mg mL^{-1} BCP in acid (pH 2) water was prepared and stirred until the copolymer was dissolved. The final solution was passed through a 0.2 µm nylon filter to remove any impurities. The self-assembly process was triggered by increasing the pH slowly to pH 8 through the addition of 1 M and 0.1 M NaOH. Finally, Empty-Psomes were formed after two or three days of stirring in dark condition. The solution was passed through a 0.8 µm nylon filter and then irradiated (photo-crosslinking) for 3 min to trigger the crosslinking to enhance its stability **Figure S3**.

In order to fabricate post-loaded HYAL-Psomes, an adopted method previously published was used.[3] Firstly, a stock solution of 1 mg mL^{-1} fresh HYAL was prepared by adding hyaluronidase from bovine testes (Type IV-S, lyophilized powder, 3000 units mg^{-1} solid, Sigma Aldrich) into the 10 mM phosphate buffered saline (PBS) contains 0.01% $\frac{W}{V}$ bovine serum albumin (BSA). Then a solution of 0.4 mg mL^{-1} HYAL was prepared in 2 mM PBS and stirred 30 min. Afterward, the solution was filtrated using 0.2 µm nylon filter. This solution was mixed with a suspension of 1 mg mL^{-1} Empty-Psomes, in 1:1 ratio to obtain the following conditions: C_{Psomes} = 0.5 mg mL^{-1} and C_{HYAL} = 0.2 mg mL^{-1} (final concentration of PBS = 1 mM). The pH of the resulting solution is adjusted to a value of 6.0 by addition of 0.1 M HCl. The suspension is left stirring in the dark for 2 h. Finally, the pH is adjusted to a value of 7.5 by addition of 0.1 M NaOH. Finally, the HYAL-Psomes solution was placed in a dialysis bag (MWCO 300 kDa) and was purified for 3 days against 1 mM PBS (the medium was changed 3 times per day). The same protocol was used for RhB-HYAL-Psomes (**Figure 4a**, main text).

Empty-Psomes and HYAL-Psomes were successfully characterized by DLS (Zetasizer Nano-series instrument, Malvern Instruments, UK), Cryo-TEM (Libra 120 microscope, Carl Zeiss Microscopy GmbH, Germany) (**Table 1**, main text). The stability and robustness were proven

after 3 pH cycles in 1 mM PBS **(Figure S4a)**. The increase in hydrodynamic diameter due to the incorporation of the enzyme into the membrane can be observed by DLS as well (**Figure S4b** and **Table S2**). As we can in **Figure S4b**, the pH* value (critical pH value- semi swollen state) was shifted from 6.77 (Empty-Psomes) to 6.96 (HYAL-Psomes). Moreover, the swollen and collapsed states are not sharp as in the case of the empty-Psomes. It is due to the presence of the enzyme in the membrane and on the surface leaving pseudo-collapsed states, which could allow to have the enzyme available without a release on demand.

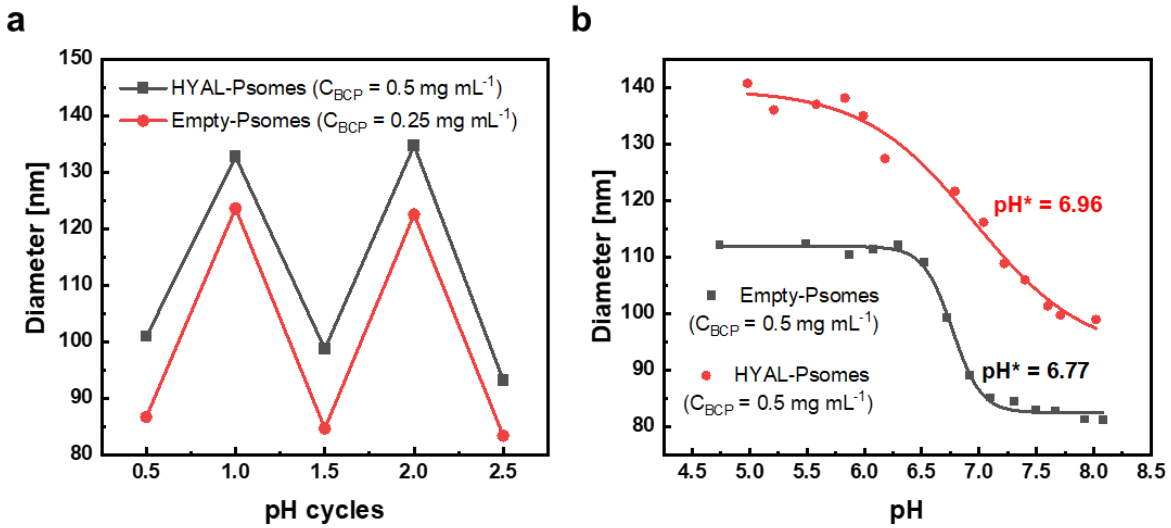

Figure S4. a) pH cycles and b) pH titration by DLS in 1 mM PBS using Empty-Psomes and purified HYAL-Psomes.

Table S2. DLS measurements in 1 mM PBS at pH 8 (C_{BCP} = 0.5 mg mL^{-1})

Samples	Diameter (nm)	PDI
Empty-Psomes	81.2	0.222
Unpurified HYAL-Psomes	90.6	0.135
Purified HYAL-Psomes	100.9	0.181
Unpurified RhBHYAL-Psomes	88.5	0.136
Purified RhBHYAL-Psomes	98.6	0.158

Preparation and characterization of labeled enzyme solution (RhB-HYAL)

5 mg of the enzyme were dissolved in 1 mL of buffer (PBS 10 mM, pH 9) and 29 µL of RhB-SCN solution (1.5 mg RhB-SCN in 150 µL DMSO). The solution was stirred in the dark area overnight. The solution was purified by dialysis (20 kDa) for 24 h against 1 mM PBS (3 times

change in 1 day) **Figure S5**. The calibration curve of the used Rhodamine B is depicted in **Figure S5**.

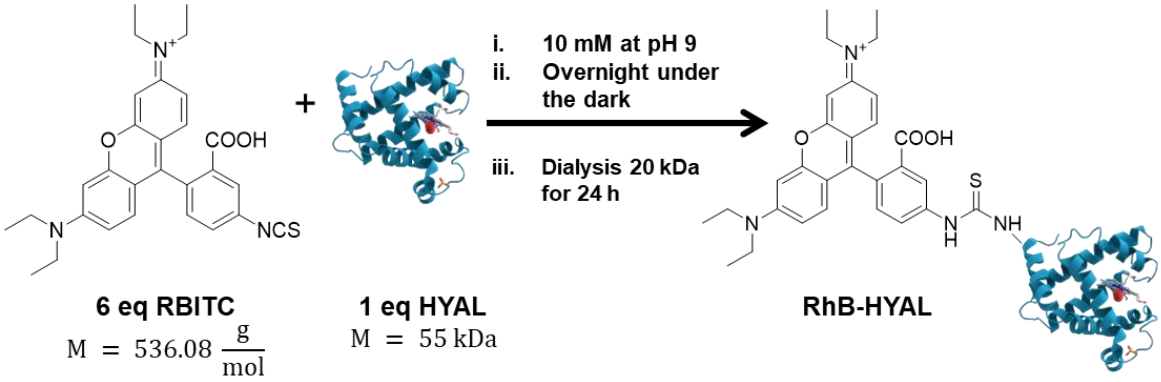

Figure S5. Synthesis of labeled enzyme with Rhodamine B (RhB-HYAL).

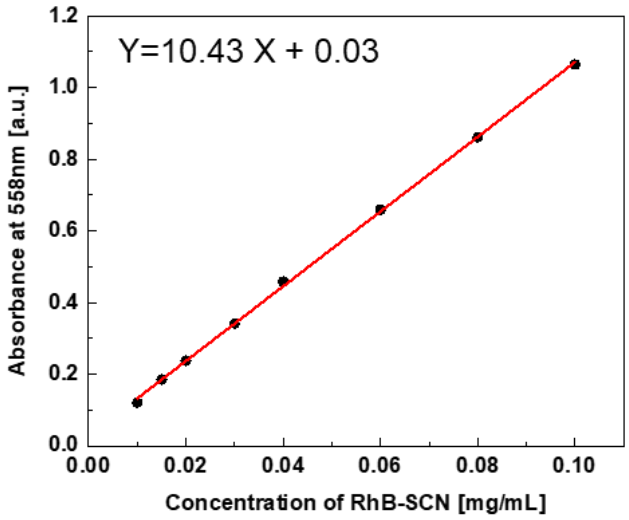

Figure S6. Calibration curve of RhB-SCN by UV-VIS spectroscopy (tor triplicate replications).

After post-loading of RhB-HYAL-Psomes, three days of purification via dialysis process carried out (MWCO 300 kDa membrane). During the dialysis, every day, 1 mL of solution extracted and kept in dark area for further fluorescence spectroscopy (FS5 spectrofluorometer, Edinburgh Instruments Ltd., U.K).

Enzymatic assay of HYAL for enzyme activity measurement

To estimate enzyme activity in different stage, before and after post-loading, the enzyme assays (modified from Enzymatic Assay of Hyaluronidase (3.2.1.35), Sigma Aldrich) were carried out.

Preparation of enzyme solution: For each desired concentration of enzyme solution, the hyaluronidase from bovine testes (Type IV-S, lyophilized powder, 3000 units mg^{-1} solid, Sigma Aldrich) was dissolved into the 10 mM phosphate buffered saline (PBS) contains 0.01% $\frac{w}{v}$ bovine serum albumin (BSA). The pH adjusted to 7 and the solution was incubated for 1 h, afterward filtrated using NY 0.2 µm.

Preparation of Hyaluronic Acid Solution 0.06% $\frac{W}{V}$: 6 mg hyaluronic acid (HA) were dissolved in 10 mL of 10 mM PBS. The solution was heat (90-95°C) and stirred for 45 min. Afterward, the solution was cool down and the pH was adjusted at pH 7 (using 0.1 M NaOH or 0.1 M HCl).

Preparation of Acidic Albumin Solution 1 mg mL^{-1}: 150 mg of BSA were dissolved in 3.6 mL of sodium acetate (1 M, pH 4.8) and 0.68 mL acetic acid. The volume was adjusted to 150 mL using Millipore water. The pH was adjusted to 3.75 (using 0.1 M NaOH or 0.1 M HCl).

Stability study of RhB-HYAL-Psomes in different pH

After complete purification (72 h of dialysis), four purified HYAL-Psomes solution (C_{Psomes} = 0.5 mg mL^{-1} and C_{HYAL} = 0.2 mg mL^{-1}) were incubated at RT in pH 5, 6, 7 and 8 inside dialysis bag for 1 h (the estimation time of fertilization process). Afterward, the dialysis media change to pH 7.5 and purified for 24 h against 1 mM PBS (MWCO 300 kDa membrane). The absorbance of the solutions was measured by fluorescence spectroscopy (Ex=554 nm, Em=575 nm) (FS5 spectrofluorometer, Edinburgh Instruments Ltd., U.K).

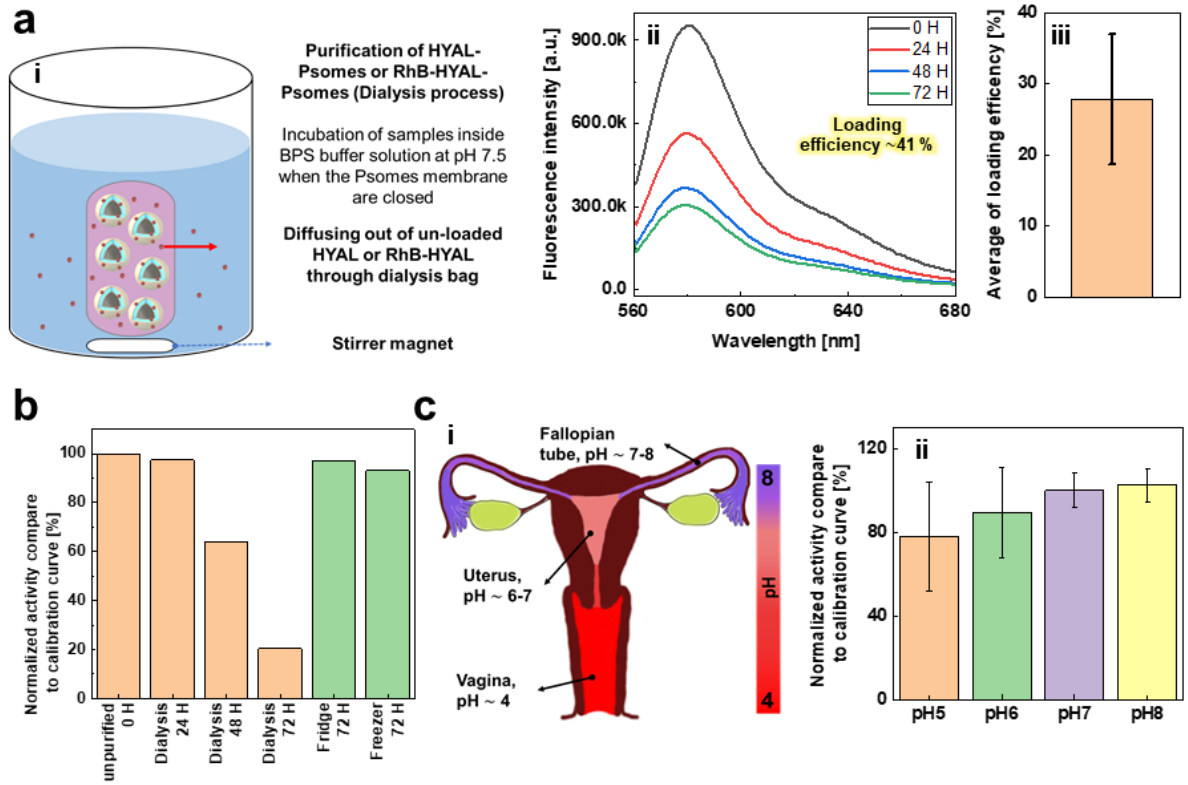

1025

1026 **Figure S7.** a) Loading efficiency of RhB-HYAL-Psomes, (i) Schematic of dialysis process, (ii)
1027 Fluorescence spectroscopy of RhB-HYAL-Psomes during purification process, (iii) Average loading
1028 efficiency (n=10, mean, ±SD), b) Normalized activity of unpurified HYAL-Psomes at different storage
1029 conditions and monitoring of dialysis process (n=6, N=1, mean); reference is unpurified sample before
1030 dialysis (=0 H), c) (i) Schematic of natural pH changes in the female reproductive tract, (ii) Normalized
1031 activity of purified HYAL-Psomes after dialysis for 24 h against different pH values (n=4, N=3, mean,
1032 ±SD); reference is purified sample before additional dialysis (=72 H).

1033 *Enzyme activity test*: Using 0, 1, 2, 4, 6, 8, and 10 µg mL^{-1} of fresh enzyme solution. For free
1034 enzyme and HYAL-Psomes, a stock solution of 0.02 mg mL^{-1} was prepared. Different amounts
1035 of enzyme, buffer and HA were added **(Table S3)**. The solutions were incubated at 38 °C for
1036 90 min. After incubation, 25 µL of each sample and Blank were added into 125 µL of Acidic
1037 Albumin Solution (96 well plate) and incubated for 30 min. Then optical density of triple
1038 measurements per each concentration at 600 nm with a TECAN infinite PRO microplate reader
1039 were determined **Figure S8**.

1040 **Table S3.** Preparation of different enzyme concentration for enzymatic assay.

Enzyme Concentration (µg mL^{-1})	0	1	2	4	6	8	10
Enzyme solution (0.02 mg mL^{-1})	0	50	100	200	300	400	500

V (µL)	PBS 10 mM	500	450	400	300	200	100	0
	HA	500	500	500	500	500	500	500

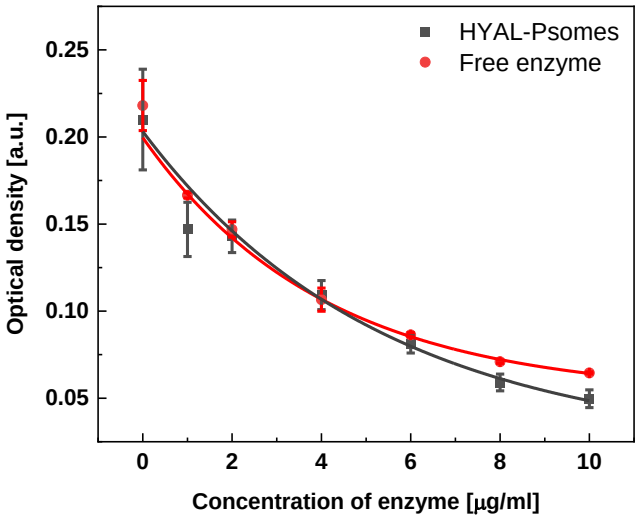

Figure S8. Calibration curves of free enzyme and unpurified HYAL-Psomes (N=3, mean, ±SD).

pH and temperature through the female reproductive tract

The pH gradient in the female reproductive tract gradually increased from the vagina (~pH 4.42) toward the fallopian tubes (FTs) (~pH 7.94) (**Table S4**). Accordingly, in our work, we considered the pH range from 5 to 8 for the stability study of enzymes loaded on pH-sensitive polymersomes.

Table S4. The pH within the female reproductive tract

Location (spacious)	**Median pH value**	**References**
Vagina (Human)	4.42	[4]
Cervix (Human)	7	[5]
Uterus (Bovine, Rabbit)	7.35, 7.47	[6], [7]
Fallopian tube (Rabbit)	7.94	[8]

The temperature through the female reproductive tract is affected by many factors, such as different phases of the female ovulation cycle, the thermogenic action of progesterone, and other internal or external components.[9] As listed in **Table S5**, each part of the female reproductive tract has a specific temperature that should be considered for future in vivo applications. On the other hand, in some works, people studied the temperature response of human sperm in a wide range of temperature changes from 34°C-39°C or 29°C-41°C.[10], [11]

So, in our work, we considered a physiologically relevant temperature range from 35°C to 40°C, not only to make sure that we studied everything close to the in vivo conditions but also to be comparable with existing studies in vitro. Notably, our proposed microcarrier needs to be optimized and improved to be able to transfer to living animals under natural conditions.

Table S5. The temperature within the female reproductive tract

Location (spacious)	Temperature value [°C]	References
Vagina (Human)	36.7-37.2	[12], [13]
Fallopian tube (isthmus, ampulla) (Rabbit)	34.7-36.3	[14]
Ovary (Pig)	35.6-37.3	[15]

Immobilization of HYAL-Psomes on the microcarrier's surface

To immobilize HYAL-Psomes on the microcarrier's surface, first thin layer of SiO_2 (20 nm) was coated onto the microcarrier arrays for the further surface functionalization process. After activating the SiO_2-coated microcarriers with oxygen plasma (1 min, 95% power), the sample was incubated overnight with 2% carboxyethylsilantriol. Afterward, the sample was washed properly with DI water. Then the sample was immersed in the solution contains: 0.05 M β-CD (6-Monoamino-6-monodexy-β-Cyclodextrin HCl), 0.1 M EDC (1-Ethyl-3-(3-dimethylaminopropyl)carbodiimide), and 0.05 M NHS (N-Hydroxysuccinimide) in 1 mL PBS (10 mM, at pH 9) and left it for overnight incubation at RT. By help of EDC and NHS the β-CD molecules were attached onto the surface. After washing process with DI water, the sample was ready for non-covalent reaction between β-CD and PEG chains of HYAL-Psomes (or RhB-HYAL-Psomes) based on a hydrophobicity reaction (2 h of incubation, pH=7.4, $C_{HYAL\text{-}Psomes}$ = 0.5 mg mL^{-1}) (**Figure 4b**, main text).

Qualitative study of cumulus cell removal

In Figure S9a.i, for only cumulus cells (murine samples) in the cell medium after 30 min of incubation, there was no evidence of extracellular digestion (separation of individual cells from the main cluster). In Figure S9a.ii, we added HYAL into the cell medium with a final concentration of 0.04 µg/mL. In this case, it was observed that after incubation which we showed in smaller time intervals (0, 10, 15, and 30 min) (Figure S9b), the extracellular matrix of hyaluronic acid was digested by hyaluronidase, and cells were separated from the main

cluster. After 30 min of incubation, the extracellular matrix was completely digested. In Figure S9a.iii, we added non-immobilized microcarriers, in which there was no change in the cumulus complex after 30 min of incubation. Finally, we added microcarriers immobilized with HYAL-Psomes (Figure S9a.iv), where we observed a slight cell spreading after incubation (the location of the cumulus cluster was indicated with the red arrow in the figure). We repeated these steps for bovine cumulus complex (**Figure S9c**), where we observed the same trend of cumulus removal compare to the murine samples (**Figure S9a,b**).

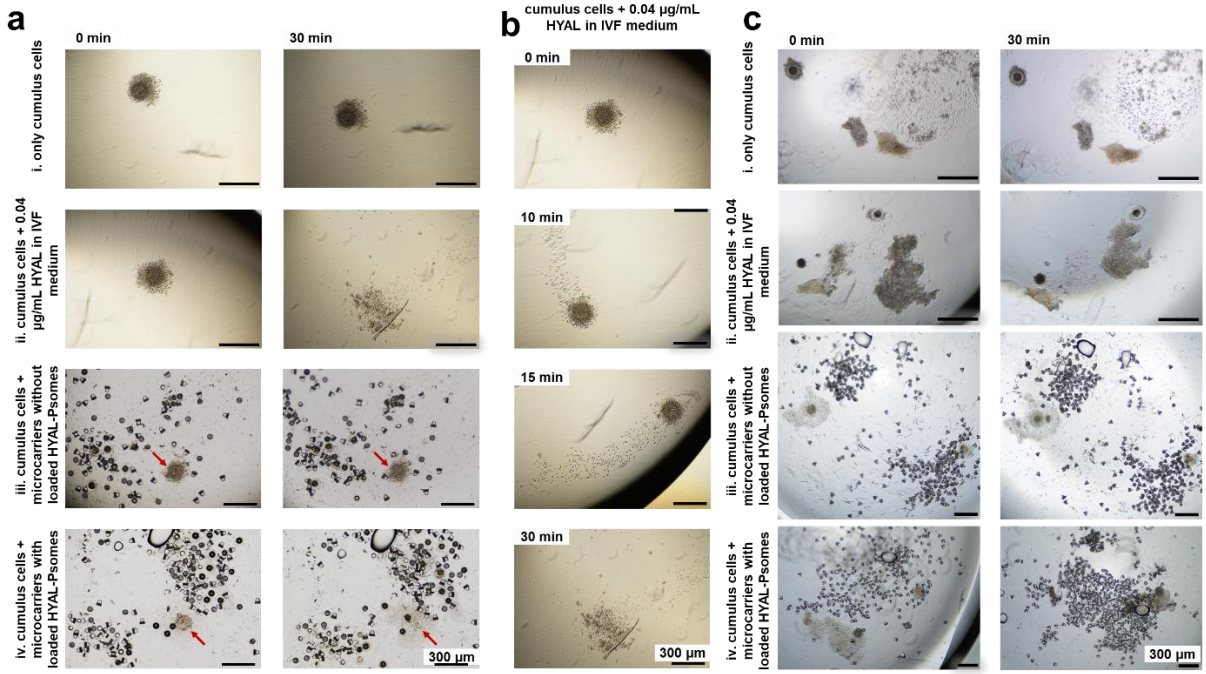

Figure S9. A qualitative study of the concept of the extracellular digestion of cumulus complex; in murine samples: a) (i) only cumulus cells after 30 minutes of incubation at 38°C, (ii) cumulus cells in 0.04 µg/mL of HYAL in the cell medium, (iii) cumulus cells in presence of non-loaded microcarriers, and (iv) cumulus cells in presence of HYAL-Psomes loaded microcarriers (the location of the cumulus cluster is pointed by red arrow) ($n_{microcarriers} > 50$), b) cumulus cells in 0.04 µg/mL of HYAL in the cell medium after 0, 10, 15, 30 min incubation at 38°C; in bovine samples: c) (i) only cumulus cells after 30 minutes of incubation at 38°C, (ii) cumulus cells in 0.04 µg/mL of HYAL in the cell medium, (iii) cumulus cells in presence of non-loaded microcarriers, and (iv) cumulus cells in presence of HYAL-Psomes loaded microcarriers (the location of the cumulus cluster is pointed by red arrow) ($n_{microcarriers} > 50$).

The magnetic field flux of an external hand-held magnet:

We calculated the magnetic field flux of a hand-held permanent magnet by using a Hall sensor. **Figure S10** shows at a 2 cm distance from the magnet we have ca.22 mT of magnetic field flux, which is ca. 540 mT at zero distance.

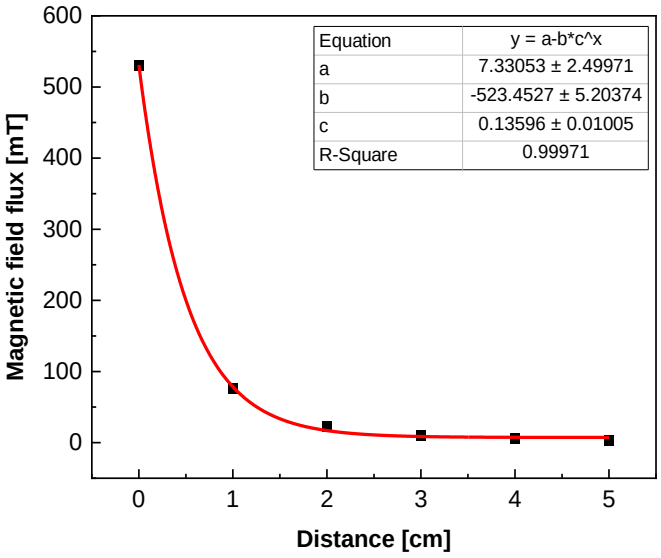

Figure S10. The magnetic field flux of an external hand-held magnet was measured using a Hall sensor from 0 to 5 cm distance.

Hybrid ultrasound (US) and photoacoustic (PA) Imaging

Device: FUJIFILM VisualSonics, The Netherlands. The measurements were carried out using a 256-elements linear array US transducer at a central frequency of 21 MHz and the captured data were collected and reconstructed using on-board post-processing. The images were further optimized by adjusting the gain to achieve better visualization of the moving microcarriers.

Phantom tubing: we used phantom tube with inner diameter ~380 µm and outer diameter ~840 µm from SAI Infusion Technologies, USA.

Experiment: The microcarriers (15-20 µL solution) were inserted into the tube and immersed in the DI water bathtub for better acoustic coupling. The sample was illuminated in the near-infrared range (800 nm) and after the PA acquisition, the spectral characteristics of the samples were recorded. The laser power density was set below the Maximum Permissible Exposure (MPE) limit (20 mJ cm^{-2}) followed by the safe exposure guidelines, US image quality is influenced by the spatial resolution and medium through which sound travels from the transducer.[16]

Ligh-to-heat conversion during imaging process

In this work, we employed a very thin Au layer of 20 nm Au which was not in direct contact to the PNIPAM microgate. There was an IPS photoresist body and an Fe layer in between. Additionally, the laser power employed for imaging was below the safety limits (800 nm, 20 mJ/cm^2, 20 Hz) and will be irradiated through scattering tissues when applied in vivo, decreasing the laser intensity much further when reaching the microcarrier location. So, it is assumed that the local heat transfer is not efficient to raise the temperature required to induce a shape change in the PNIPAM microgate (T ≅ 5°C), that releases the sperm cells and heparin before reaching the target location.

To confirm this assumption, we measured the light absorbance of the Au-coated sperm microcarriers in the wavelength range from 500 to 1100 nm (including the traditional bioimaging window ranging from 760 to 900 nm), using differential reflectance spectroscopy (DRS) (Analytik Jena, SPECORD 250). We compared the absorption spectrum from microcarriers with and without the gold layer in an aqueous solution (ca. 12500 microcarriers per mL in 1mM PBS). In Figure S11,a we observed that the major absorption peak occurs at a wavelength of 980 nm (different to the wavelength selected for our preliminary photoacoustic imaging experiments, 800 nm). Based on the obtained absorption properties of our sperm microcarriers and the applied experimental conditions, we calculated the heat flux (Equation S1) and temperature change (Equation S2) to determine if such phototermal effect could have an influence on the PNIPAM microgate actuation. For that we employed an already reported model by Paściak and coauthors).[17]

$$Q_A = I_0(1 - 10^{-A})\eta_Q \qquad \text{Equation S1}$$

$$Q_A = C_a \Delta T \qquad \text{Equation S2}$$

In the above-mentioned equations, (Q_A) is heat produced by converting the absorbed light into heat, (I_0) is the intensity of the incident light (at 800 nm, 20mJ/cm^2, 20 Hz), (A) is the absorbance of the sperm-microcarrier at 800 nm (0.13 a.u.), (η_Q) is light-to-heat conversion coefficient (0.508) [17], and (C_a) is the specific heat capacity (for gold 129 J/°C). As shown in Figure R4b (new Figure S11, b), the temperature change per cm^2 is ca.0.5°C at the wavelength of 800 nm for a continuous light exposure during ca. 6h (the time sperm cells are motile), which is not sufficient to induce a significant PNIPAM shape change. It is also noteworthy mentioning that in our calculations, we ignored heat produced by converting the absorbed light into heat in the solution which could equilibrate the total heat conversion and reduce the final temperature

change. Also the response to the PNIPAM will depend on the LCST, which can be further tuned depending on the in vivo conditions.

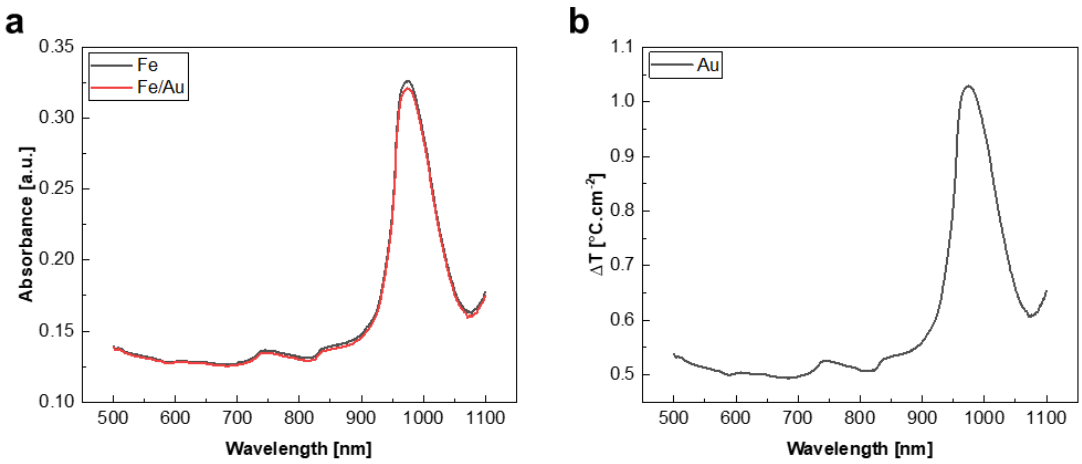

Figure S11. a) Differential reflectance spectroscopy of microcarriers with and without 20nm of Au layer in an aqueous solution (PBS, 1mM), b) Calculated temperature gradient per cm^2 of microcarriers with Au layer in an aqueous solution.

2. Statistical analysis

For MTS-assay (Figure 1d) ca. 5000 cells per each well were cultured (in a 96-well microtiter plate) in 6 replications per each condition including (control, IPS, IPS/PNIPAM, IPS/PNIPAM/Coating layers). Then average values with standard deviations were reported.

For temperature actuation tests (Figure 2), the change of the surface area was measured per each microcube or microgate, over 1, 2 or 3 temperature cycles (dependce on the experiment), and measured values were reported.

For curvilinear, average path velocities, and motility measurments were analyzed by computer-assisted sperm analysis (CASA, AndroVision®, Minitub GmbH, Germany). We kept the number of sperm cells per each condition ca. 200 with at least triplicate repititions. Then average values with standard deviations were reported.

For the spectrophotometry experiments we kept the number of replications per each condition equal 3. Respectively, for all calibration curves and absorbance intensity measurments we reported the avarage values with standard deviations.

Reference

[1] J. Gaitzsch, D. Appelhans, L. Wang, G. Battaglia, and B. Voit, "Synthetic Bio-nanoreactor: Mechanical and Chemical Control of Polymersome Membrane Permeability," *Angew. Chemie Int. Ed.*, vol. 51, no. 18, pp. 4448–4451, Apr. 2012, doi: 10.1002/ANIE.201108814.

[2] S. Moreno *et al.*, "Light-Driven Proton Transfer for Cyclic and Temporal Switching of Enzymatic Nanoreactors," *Small*, vol. 16, no. 37, p. 2002135, Sep. 2020, doi: 10.1002/SMLL.202002135.

[3] E. Geervliet *et al.*, "Matrix metalloproteinase-1 decorated polymersomes, a surface-active extracellular matrix therapeutic, potentiates collagen degradation and attenuates early liver fibrosis," *J. Control. Release*, vol. 332, pp. 594–607, Apr. 2021, doi: 10.1016/J.JCONREL.2021.03.016.

[4] F. Peeters, R. Snauwaert, J. Segers, J. van Cutsem, and W. Amery, "Observations on candidal vaginitis," *Am. J. Obstet. Gynecol.*, vol. 112, no. 1, pp. 80–86, Jan. 1972, doi: 10.1016/0002-9378(72)90533-9.

[5] W. Eggert-Kruse, H. Hofmann, I. Gerhard, A. Bilke, B. Runnebaum, and D. Petzoldt, "Effects of antimicrobial therapy on sperm-mucus interaction*," *Hum. Reprod.*, vol. 3, no. 7, pp. 861–869, Oct. 1988, doi: 10.1093/oxfordjournals.humrep.a136798.

[6] E. C. Mather, "'In vivo' uterine lumen pH values of the bovine," *Theriogenology*, vol. 3, no. 3, pp. 113–119, Mar. 1975, doi: 10.1016/0093-691X(75)90160-0.

[7] B. G. Brackett and L. Mastroianni, "Composition of oviducal fluid," in *The Oviduct and its Functions*, University of Chicago Press, 1974, pp. 231–250.

[8] D. H. A. Maas, B. Stein, and H. Metzger, "Po2 and pH Measurements within the Rabbit Oviduct Following Tubal Microsurgery: Reanastomosis of Previously Dissected Tubes," in *Advances in experimental medicine and biology*, vol. 169, Adv Exp Med Biol, 1984, pp. 561–570.

[9] K. Y. B. Ng, R. Mingels, H. Morgan, N. Macklon, and Y. Cheong, "In vivo oxygen, temperature and pH dynamics in the female reproductive tract and their importance in human conception: a systematic review," *Hum. Reprod. Update*, vol. 24, no. 1, pp. 15–

34, Jan. 2018, doi: 10.1093/humupd/dmx028.

[10] A. Bahat, S. R. Caplan, and M. Eisenbach, “Thermotaxis of Human Sperm Cells in Extraordinarily Shallow Temperature Gradients Over a Wide Range,” *PLoS One*, vol. 7, no. 7, p. e41915, Jul. 2012, doi: 10.1371/journal.pone.0041915.

[11] S. Pérez-Cerezales *et al.*, “Involvement of opsins in mammalian sperm thermotaxis,” *Sci. Rep.*, vol. 5, no. 1, p. 16146, Dec. 2015, doi: 10.1038/srep16146.

[12] G. A. Yedwab, G. Paz, T. Z. Homonnai, M. P. David, and P. F. Kraicer, “The Temperature, pH, and Partial Pressure of Oxygen in the Cervix and Uterus of Women and Uterus of Rats During the Cycle,” *Fertil. Steril.*, vol. 27, no. 3, pp. 304–309, Mar. 1976, doi: 10.1016/S0015-0282(16)41722-X.

[13] J. T. Samples and R. M. Abrams, “Reliability of Urine Temperature as a Measurement of Basal Body Temperature,” *JOGN Nurs.*, vol. 13, no. 5, pp. 319–323, Sep. 1984, doi: 10.1111/j.1552-6909.1984.tb01146.x.

[14] A. Bahat, M. Eisenbach, and I. Tur-Kaspa, “Periovulatory increase in temperature difference within the rabbit oviduct,” *Hum. Reprod.*, vol. 20, no. 8, pp. 2118–2121, Aug. 2005, doi: 10.1093/humrep/dei006.

[15] R. H. F. Hunter, C. Grondahl, T. Greve, and M. Schmidt, “Graafian follicles are cooler than neighbouring ovarian tissues and deep rectal temperatures,” *Hum. Reprod.*, vol. 12, no. 1, pp. 95–100, Jan. 1997, doi: 10.1093/humrep/12.1.95.

[16] R. J. Thomas, B. A. Rockwell, W. J. Marshall, R. C. Aldrich, S. A. Zimmerman, and R. J. R. Jr., “A procedure for multiple-pulse maximum permissible exposure determination under the Z136.1-2000 American National Standard for Safe Use of Lasers,” *J. Laser Appl.*, vol. 13, no. 4, p. 134, Jul. 2001, doi: 10.2351/1.1386796.

[17] A. P. Paściak, A. Pilch-Wróbel, Ł. Marciniak, P. J. Schuck, and A. Bednarkiewicz, “Standardization of Methodology of Light-to-Heat Conversion Efficiency Determination for Colloidal Nanoheaters,” Cite This ACS Appl. Mater. Interfaces, vol. 13, pp. 44556–44567, 2021, doi: 10.1021/acsami.1c12409.